

# Saturn's Seasonal Atmosphere at Northern Summer Solstice

L.N. FLETCHER<sup>1</sup>, L. SROMOVSKY<sup>2</sup>, V. HUE<sup>3</sup>, J.I. MOSES<sup>4</sup>, S. GUERLET<sup>5</sup>, R.A. WEST<sup>6</sup>, AND T. KOSKINEN<sup>7</sup>

<sup>1</sup> School of Physics and Astronomy, University of Leicester, University Road, Leicester, LE1 7RH, UK.

<sup>2</sup> Space Science and Engineering Center, University of Wisconsin, Madison, WI 53706, USA.

<sup>3</sup> Southwest Research Institute, Department of Space Science, Space Science and Engineering Division, 6220 Culebra Road, San Antonio, TX 78238-5166, USA.

<sup>4</sup> Space Sciences Institute, 4765 Walnut St, Suite B, Boulder, CO 80301, USA.

<sup>5</sup> Laboratoire de Meteorologie Dynamique / CNRS / Sorbonne Université, 4 Place Jussieu, 75252 Paris, France.

<sup>6</sup> NASA Jet Propulsion Laboratory, 4800 Oak Grove Drive, Pasadena, CA 91109, USA.

<sup>7</sup> Lunar and Planetary Laboratory, University of Arizona, 1629 E. University Blvd., Tucson, AZ 85721, USA.

## Copyright Notice

The Chapter, "Saturn's Seasonal Atmosphere at Northern Summer Solstice", is to be published by Cambridge University Press as part of a multi-volume work edited by Kevin Baines, Michael Flasar, Norbert Krupp, and Thomas Stallard, entitled "Cassini at Saturn: The Grand Finale" ('the Volume')

© in the Chapter, L.N. Fletcher, L. Sromovsky, V. Hue, J.I. Moses, S. Guerlet, R.A. West and T. Koskinen,

© in the Volume, Cambridge University Press

NB: The copy of the Chapter, as displayed on this website, is a draft, pre-publication copy only. The final, published version of the Chapter will be available to purchase through Cambridge University Press and other standard distribution channels as part of the wider, edited Volume, once published. This draft copy is made available for personal use only and must not be sold or re-distributed.

## Abstract

The incredible longevity of Cassini's orbital mission at Saturn has provided the most comprehensive exploration of a seasonal giant planet to date. This review explores Saturn's changing global temperatures, composition, and aerosol properties between northern spring and summer solstice (2015-2017), extending our previous review of Cassini's remote sensing investigations (2004-2014, [Fletcher et al., 2018b](#)) to the grand finale. The result is an unprecedented record of Saturn's climate that spans almost half a Saturnian year, which can be used to test the seasonal predictions of radiative climate models, neutral and ion photochemistry models, and atmospheric circulation models.

Hemispheric asymmetries in tropospheric and stratospheric temperatures were observed to reverse from northern winter to northern summer. Spatial distributions of hydrocarbons and para-hydrogen shifted in response to atmospheric dynamics (e.g., seasonally-reversing circulations, polar stratospheric vortex formation, equatorial stratospheric oscillations, and inter-hemispheric transport). Upper tropospheric and stratospheric aerosols exhibited changes in optical thickness that modulated Saturn's visible colours (from blue hues to a golden appearance in the north near solstice), reflectivity, and near-infrared emission. Numerical simulations of radiative balance and photochemistry effectively reproduce the observed seasonal change and phase lags, but discrepancies between models and data still persist, indicating a crucial role for atmospheric dynamics and the need to couple chemical and radiative schemes to the next generation of circulation models. With Cassini's demise, an extended study of Saturn's seasons, from northern summer to autumn, will require the capabilities of ground- and space-based observatories, as we eagerly await the next orbital explorer at Saturn.

## 11.1 Introduction: Cassini's First Decade

Over thirteen years of unprecedented orbital exploration, the Cassini spacecraft provided our first comprehensive characterisation of the seasonal evolution of a Giant Planet atmosphere. Its remote sensing investigations explored the shifting temperatures, aerosol properties, and spatial distributions of gaseous species, revealing the delicate interplay between atmospheric circulation, photochemistry, radiative heating/cooling, and cloud microphysics. Given Saturn's 26.7° axial tilt and 29.5-year orbit, only a long-lived orbiting spacecraft could monitor these processes over seasonal timescales, providing access to both the sunlit summer hemisphere and the darkness of Saturn's winter. In [Fletcher et al. \(2018b\)](#), we reviewed our knowledge of the physical and chemical processes shaping the seasonal giant during the first decade of Cassini observations (2004-2014). The Cassini results were compared to ground-based (e.g., [Gillett and Orton, 1975](#); [Gezari et al., 1989](#); [Orton and Yanamandra-Fisher, 2005](#); [Greathouse et al., 2005](#)), Pioneer 11 ([Orton and Ingersoll, 1980](#)), and Voyager ([Hanel et al., 1981, 1982](#)) infrared observations of thermal emission, and reflected sunlight measurements from Hubble and Earth-based observers

(e.g., Karkoschka and Tomasko, 1992; Stam et al., 2001; Pérez-Hoyos et al., 2005; Karkoschka and Tomasko, 2005) from the mid-1970s to the early 21st century.

Cassini arrived at Saturn in July 2004, shortly after northern winter solstice in October 2002 (a heliocentric solar longitude  $L_s = 270^\circ$ ), and its prime and extended missions monitored atmospheric changes through northern spring equinox in August 2009 ( $L_s = 0^\circ$ ), and into northern mid-spring in 2014 ( $L_s \sim 55^\circ$ ). During this time, the southern summer hemisphere was receding into the darkness of autumn, and the northern winter hemisphere was emerging into sunlight for the first time in 15 years. In this review, we extend this analysis from 2015 ( $L_s \sim 60^\circ$ ) through northern summer solstice in May 2017 ( $L_s = 90^\circ$ ), all the way to the end of Cassini’s mission in September 2017 ( $L_s = 93^\circ$ ) and beyond, using ground-based observatories. This extensive seasonal coverage, which encompassed Cassini’s proximal orbits and grand finale in 2016-17, means that we have a database of Saturn’s climate spanning almost half a Saturnian year, and the period between perihelion ( $L_s = 280^\circ$ , June 2003) and aphelion ( $L_s = 100^\circ$ , April 2018).

The first decade of Cassini observations revealed hemispheric asymmetries in tropospheric and stratospheric temperatures, aerosol opacity, and chemical composition (Fletcher et al. (2018b)). These large-scale asymmetries were superimposed onto smaller-scale dynamic perturbations, such as gradients in thermal emission and reflectivity associated with the cool anticyclonic zones (equatorward of prograde jets) and warm cyclonic belts (poleward of prograde jets, Conrath and Pirraglia, 1983; Vasavada et al., 2006; Fletcher et al., 2007; Del Genio et al., 2009; Fletcher et al., 2020). In addition, the hemispheric asymmetries were perturbed by the equatorial enhancements in tropospheric phosphine (a disequilibrium species, Fletcher et al., 2009b), ammonia (the key condensable forming Saturn’s top-most clouds, Fletcher et al., 2011a; Laraia et al., 2013; Janssen et al., 2013), and para-hydrogen (a tracer of vertical motion, Fletcher et al., 2010, 2016); the response of the stratospheric composition to ring-shadowing (Guerlet et al., 2009; Sylvestre et al., 2015); the disruption generated by Saturn’s 2010-2011 northern storm (Fletcher et al., 2011b; Sánchez-Lavega et al., 2011; Fletcher et al., 2012; Moses et al., 2015; Cavalié et al., 2015); and the  $\sim 15$ -year-period oscillatory pattern in the equatorial stratosphere (Orton et al., 2008; Fouchet et al., 2008). Seasonal gradients therefore cannot be understood in isolation from the atmospheric dynamics, circulation, and chemistry, and we encourage the reader to review this chapter alongside those on atmospheric dynamics (Chapter 12, Flasar et al.), polar phenomena (Chapter 13, Sayanagi et al.), and upper atmospheric observations (Chapter 9 by Moore et al. and Chapter 10 by Koskinen et al.).

By the end of 2014, it was clear that Saturn’s atmospheric temperatures above the radiative-convective boundary (400-500 mbar) were tracking seasonal changes to insolation, and that radiative modelling (Conrath et al., 1990; Friedson and Moses, 2012; Guerlet et al., 2014) was largely successful in predicting the amplitude and phase lag of the seasonal response. There were some surprises - for example, the mid-

stratospheric seasonal response appeared to be smaller than expected (Sylvestre et al., 2015). Differences between modelled and measured temperatures are likely driven by the use of spatially-uniform hydrocarbons in the models (key stratospheric coolants), by residual-mean circulation resulting in adiabatic heating and cooling, and also by simplistic assumptions about aerosol contributions to radiative balance. Indeed, aerosol variability may play a key role, and by the end of 2014, Cassini’s visible-light cameras had revealed the shifting colours of Saturn’s springtime hemisphere (Fig. 11.1), from blue hues to the more familiar yellow-ochre appearance. However, only limited quantitative studies had been performed to assess Saturn’s aerosols at single epochs with Cassini (Roman et al., 2013; Fletcher et al., 2011a; Sromovsky et al., 2013, 2020b), and no synthesis of seasonal variations had been presented. Furthermore, there was suggestive evidence of interannual variability in the temperature structure, as comparisons of measurements from Voyager 1 (1980,  $L_s = 8.6^\circ$ ) and 2 (1981,  $L_s = 18.2^\circ$ ) with Cassini at the same point in the seasonal cycle (2009-10) revealed some unexpected differences, particularly at the equator (Li et al., 2013; Sinclair et al., 2014; Fletcher et al., 2016). As we show below, the extension of Cassini’s lifetime to northern summer solstice and beyond proved to be of great benefit in understanding the timescales for these atmospheric changes.

Our previous review of Saturn’s seasons therefore left a number of open questions, particularly concerning the expected seasonal evolution between mid-spring and summer in the northern hemisphere. Although Cassini had tracked atmospheric temperatures over a full decade, the expected development of a warm north polar stratospheric vortex had not yet started (Fletcher et al., 2015). Furthermore, there was limited evidence for reversing hemispheric asymmetries in tropospheric and stratospheric composition and aerosols, raising the question of whether some hemispheric asymmetries were permanent. Neutral photochemistry modelling (Moses and Greathouse, 2005; Hue et al., 2015) had predicted the magnitude of hemispheric contrasts for a range of hydrocarbons, but remaining discrepancies between models and data hinted at the influence of stratospheric circulation. As we show in this chapter, a more complete dataset of seasonally-changing temperatures and hydrocarbons substantially improves our ability to test the predictions of radiative-convective and photochemical models.

This chapter reviews Saturn’s seasonal development since 2014, and is organised as follows. The next Section reviews the ongoing evolution of Saturn’s temperatures (Section 11.2), in comparison to expectations from radiative-climate and general circulation models. Section 11.3 then explores seasonal changes in tropospheric and stratospheric composition and compares measurements to the state of the art in seasonal chemical modelling. Section 11.4 discusses the observed changes in the properties of Saturn’s clouds and hazes. Finally, Section 11.5 describes the next stages in our exploration of Saturn’s evolution in the 2020s. The reader is referred to Fletcher et al. (2018b) for detailed descriptions of Cassini’s suite of remote sensing instruments; historical surveys of pre-Cassini observations; radiative-convective

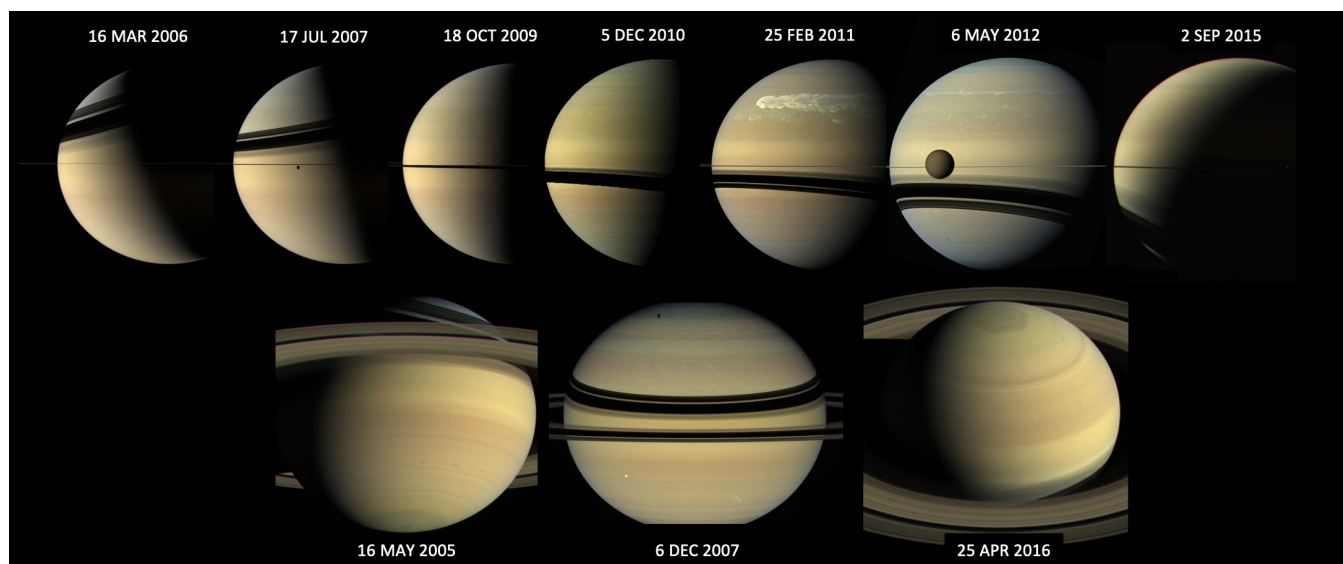


**Figure 11.1** Saturn's changing insolation from 2005 to 2016 as seen by Cassini's Imaging Science Subsystem (ISS). The top row shows Saturn from an equatorial vantage point (the rings appear edge-on), and attempts to show the location of the terminator in each image to indicate how it changed over time. The bottom row shows images from outside of the equatorial plane, showing the transition from southern summer to northern summer. Compiled from Cassini/ISS images courtesy of NASA/JPL-Caltech.

model development since the earliest equilibrium models in the 1970s; and the development of photochemical models in the troposphere (e.g., phosphine, [Visscher et al., 2009](#)) and stratosphere (e.g., methane, [Moses and Greathouse, 2005](#); [Hue et al., 2015](#)). Furthermore, this chapter will not dwell on Saturn's bulk chemical composition, for which the reader is also referred to [Fouchet et al. \(2009\)](#), nor on the influence of exogenic material on the upper atmosphere, which was reviewed in [Fletcher et al. \(2018b\)](#), and is discussed further in Chapters 9 ([Moore et al.](#)) and 10 ([Koskinen et al.](#)) based on new observations by the Cassini INMS instrument ([Waite et al., 2018](#)). Instead, we focus on those chemical species, atmospheric properties, and numerical models that provide insights into seasonal trends on Saturn near northern summer solstice.

## 11.2 Temperature Variations approaching Summer Solstice

At altitudes above the radiative-convective boundary (350–500 mbar, [Fletcher et al., 2007](#)), Saturn's upper tropospheric and stratospheric temperatures are governed by the balance between radiative heating and cooling, to first order. Heating occurs via short-wave absorption of sunlight by methane and aerosols, whereas stratospheric cooling is due to long-wave emission from ethane, acetylene, and (to a lesser extent) methane and other hydrocarbons in the mid-stratosphere ( $p < 5$  mbar), and tropospheric cooling is dominated by emission from the hydrogen-helium continuum ( $p > 5$  mbar). The amplitude of hemispheric asymmetries depends on the radiative time constant at each altitude (e.g., [Cess and Caldwell, 1979](#); [Conrath et al., 1990](#)) – when this exceeds a Saturnian year in the troposphere, the thermal field does not show seasonal asymmetries and should be close to the annual-mean radiative equilibrium values (at depths below 500–700 mbar, [Conrath and Pirraglia, 1983](#)).

When the radiative time constant is very short in the high stratosphere, the temperatures track the sub-solar point and extremes of temperature should be larger (i.e., a low thermal inertia due to having less mass at low pressures). At intermediate altitudes sensed by Cassini/CIRS, the hemispheric asymmetries in temperature lag behind the instantaneous insolation, sometimes by up to a season (e.g., [Conrath et al., 1990, 1998](#)). However, the picture is made more complicated because the key stratospheric coolants (ethane and acetylene) respond to seasonal photochemistry and are advected by circulation; the thickness, altitude, and reflectivity of tropospheric and stratospheric aerosols vary with season; and atmospheric circulation responds to large-scale temperature gradients by residual mean circulation, adiabatic heating/cooling, and wave activity. To date, no model combines the feedback processes between all of these parameters, but Cassini observations were able to constrain the temporal evolution of the various environmental parameters, albeit not over a full Saturn year.

The first decade of Cassini observations, reviewed in [Fletcher et al. \(2018b\)](#), tracked Saturn's seasonal temperature evolution beyond the first snapshots of hemispheric asymmetries ([Flasar et al., 2004](#); [Fletcher et al., 2007, 2008](#); [Guerlet et al., 2009](#)). These early studies revealed 1-mbar stratospheric temperature contrasts of  $\sim 40$  K between the summer and winter poles, decreasing to  $\sim 10$  K at the tropopause. Subsequent work revealed the cooling of the southern autumn hemisphere and the warming of the northern spring hemisphere ([Fletcher et al., 2010](#); [Li et al., 2010](#); [Sinclair et al., 2013](#); [Fletcher et al., 2015](#)), leading to almost symmetric mid-latitude 1-mbar temperatures in the

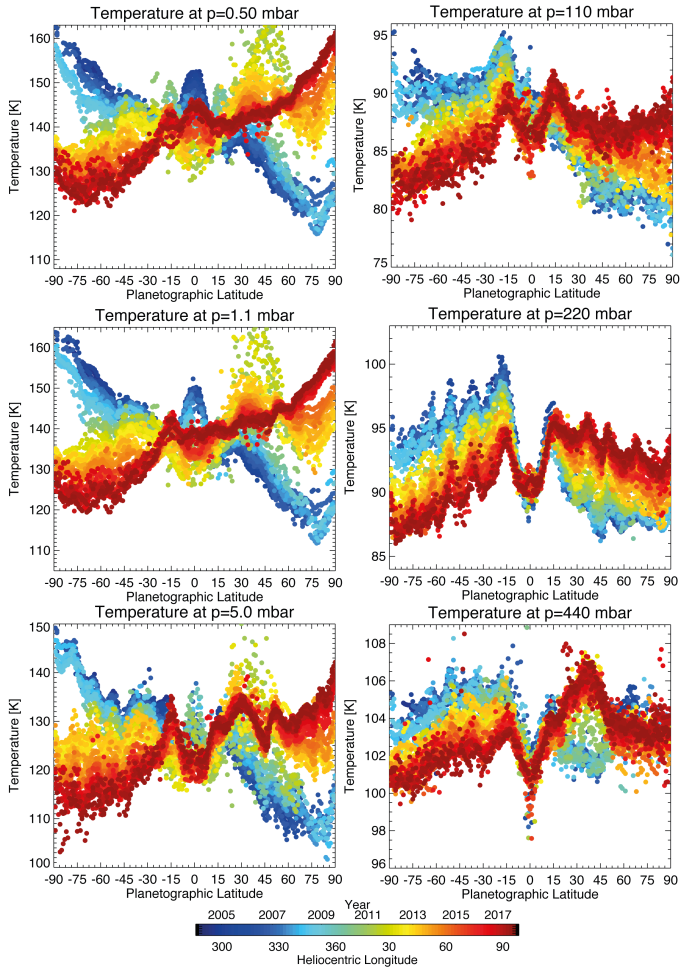


**Figure 11.2** Stratospheric (left) and tropospheric (right) temperatures derived from fitting Cassini/CIRS nadir observations using both the far-infrared (16–1000  $\mu\text{m}$ ) and mid-infrared (7–16  $\mu\text{m}$ ) focal planes (Fletcher et al., 2016, 2018a). Spectra were averaged on a monthly grid and are colour-coded according to the legend, showing the evolution from the start of Cassini’s mission (2004) to the end (2017). Note the influence of Saturn’s equatorial oscillation in the stratosphere, and the perturbations due to the 2010–2013 storm-induced stratospheric ‘beacon.’

140–145-K range by equinox. Seasonal changes were particularly apparent with the cooling and disappearance of a warm south-polar stratospheric vortex (SPSV) that had been present in the 75 – 90°S region at the start of the Cassini mission (sometimes referred to as a ‘polar hood,’ Orton and Yanamandra-Fisher, 2005; Fletcher et al., 2008, 2015). At higher stratospheric altitudes ( $\sim 0.01$  mbar), a comparison of Cassini/CIRS limb measurements between Guerlet et al. (2009) and Sylvestre et al. (2015) suggested that seasonal trends and asymmetries were less significant than those observed at 1 mbar, counter to the expectations of radiative equilibrium models.

As Saturn approached northern summer solstice in May 2017 ( $L_s = 90^\circ$ ), Cassini/CIRS continued to monitor the thermal field. A series of papers utilised CIRS nadir spectra

at the lowest spectral resolution (15  $\text{cm}^{-1}$ ), using tensioned splines to interpolate and ‘reconstruct’ Saturn’s temperatures throughout the full 13-year mission. This technique was used to investigate tropospheric seasonal change using far-IR nadir spectra (16  $\mu\text{m}$  to 1 mm, Fletcher et al., 2016); equatorial stratospheric oscillations (Fletcher et al., 2017) and polar vortices (Fletcher et al., 2018a) using mid-IR nadir spectra (7–16  $\mu\text{m}$ ). The full set of CIRS nadir temperatures in the troposphere (100–440 mbar) and stratosphere (0.5–5.0 mbar) are presented in Fig. 11.2, where each point represents an inversion of a 7–200  $\mu\text{m}$  spectrum averaged for a particular latitude and month. By northern summer solstice in 2017, the stratospheric temperatures (0.5–1.0 mbar) at high latitudes had warmed by 35 K, such that the asymmetries observed at the start of Cassini’s mission in 2004 had almost completely reversed. However, at 5 mbar in Fig. 11.2 the northern-solstice asymmetry ( $\sim 20$  K) remained smaller than that seen in 2004 ( $\sim 35$  K). The north polar region continued to warm beyond northern solstice at  $L_s = 90^\circ$  (Blake et al., 2022), so it is likely that the asymmetry had not reached its maximum in 2017. Furthermore, the different asymmetry amplitude between northern and southern solstice could be related to the small differences between perihelion (near  $L_s = 280^\circ$ ) and aphelion (near  $L_s = 100^\circ$ ) (small 2–3 K differences are observed at 0.5 mbar in radiative climate models, see below and Hue et al., 2016). This conundrum was also observed in the troposphere (110–220 mbar), where gradients reversed (and were largely symmetric by 2013–15, Fletcher et al., 2016), but the northern hemisphere would continue to warm beyond the end of Cassini’s mission. Finally, at 440 mbar (close to the radiative-convective boundary) we see seasonal changes of 4–5 K or smaller, with much of the observed variability in Fig. 11.2 driven by dynamics (see below).

The reconstructed temperature fields are shown in Fig. 11.3, revealing seasonal behaviour at both poles, switching from a cold polar vortex in winter to a warm polar vortex in summer. These figures omit the strong rise in temperatures associated with Saturn’s great northern storm that can be seen in Fig. 11.2 (Fletcher et al., 2012; Achterberg et al., 2014), whose aftermath could still be observed in the warm troposphere at 440 mbar even in 2017 (but not in the radiatively-controlled upper troposphere at  $p < 400$  mbar). The equatorial stratospheric oscillation is superimposed onto the seasonal temperature changes evident in Fig. 11.3. The banded thermal structure is apparent in the troposphere and stratosphere at 5 mbar, but less so at the 0.5–1.0 mbar level.

The changing latitudinal temperature gradients in Fig. 11.3 are related to the vertical shear of the zonal winds via the thermal wind equation (e.g., Holton, 2004). In the stratosphere, the seasonal change in the temperature gradient (from decreasing with northward latitude to increasing with northward latitude) promotes increasingly positive vertical shear on zonal jets in the southern autumn/winter stratosphere, and increasingly negative vertical shear on zonal jets in the northern spring/summer stratosphere (Friedson and Moses, 2012; Fletcher et al., 2018a). If we assume a



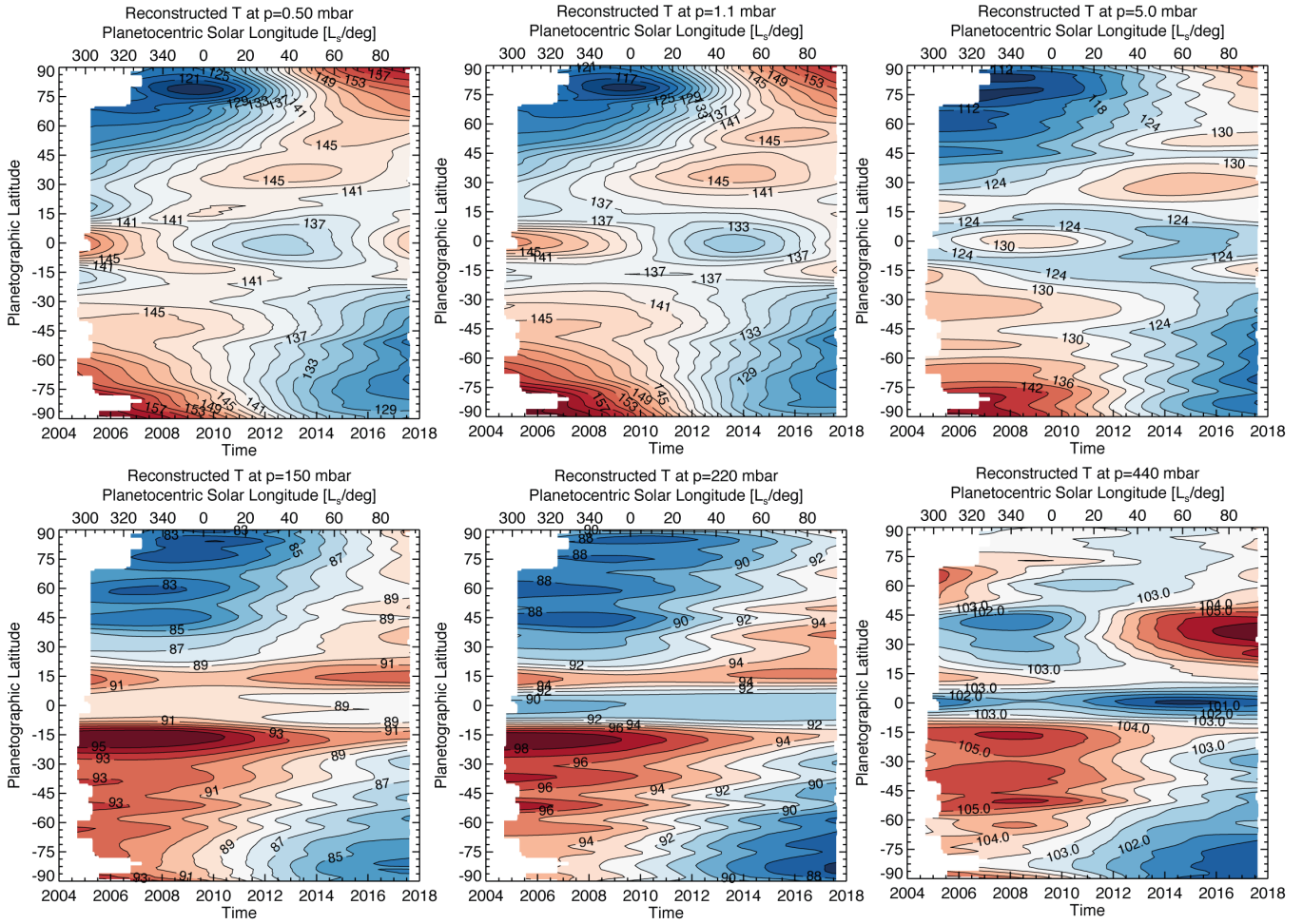


**Figure 11.3** Saturn’s stratospheric and tropospheric temperatures reconstructed from the measurements in Fig. 11.2 using tensioned splines, extending the figures in Fletcher et al. (2018a) to cover all latitudes. Whitespace at the start and end of the time series show where the measurements are unavailable (i.e., splines were used for interpolation but not extrapolation). We omitted the influence of the 2011-2013 storm at mid-latitudes in the north.

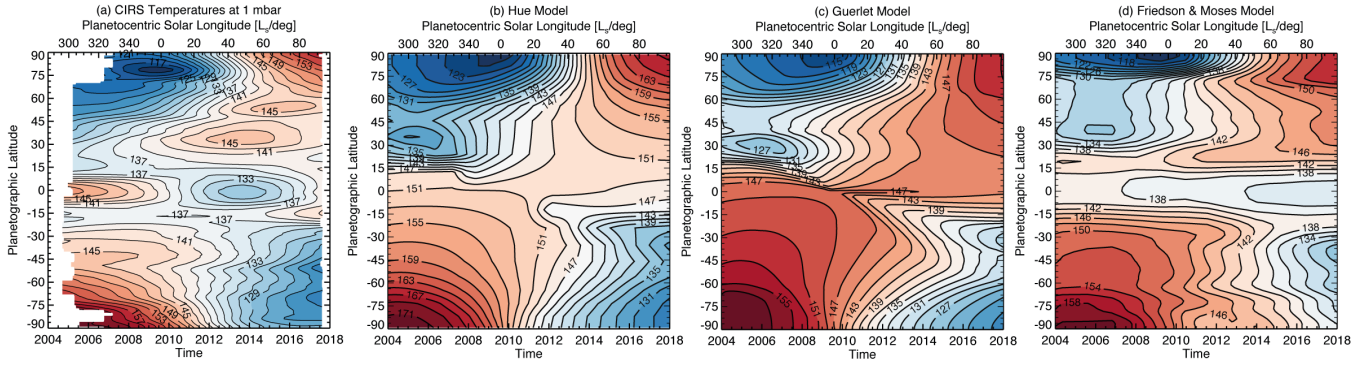
level of zero winds somewhere in the lower stratosphere, the strengthening negative windshear in the north would promote westward winds surrounding the forming north polar stratospheric vortex (NPSV), particularly at 5 mbar near  $78^\circ\text{N}$  after 2014. The NPSV also exhibited a hexagonal boundary in the stratosphere, mirroring that in the troposphere (Fletcher et al., 2018a). Similarly, the weakening of the westward winds in the south (particularly near  $74^\circ\text{S}$ ) corresponded to the disappearance of the SPSV after 2013-14. Ground-based imaging revealed that the NPSV continued to warm (therefore strengthening the circumpolar westward windshear) between 2017 and 2022 (Blake et al., 2022).

### 11.2.1 Simulating Seasonal Variability

*How well are these seasonal changes captured by radiative-convective (RC) and global climate models?* Fig. 11.4 compares the CIRS 1-mbar temperature field with predictions from three numerical models of differing complexity. Friedman and Moses (2012) described the Outer Planet General Circulation Model (OPGCM), which tracks radiative heating and cooling and accounts for dynamical redistribution of heat via adiabatic expansion/compression. Guerlet et al. (2014) developed the RC model that was incorporated into

the GCM of Spiga et al. (2020), itself extended to the upper stratosphere in Bardet et al. (2021) — we show the RC estimates of seasonal temperatures here. In both cases, the spatial distributions of hydrocarbons were treated as latitudinally and temporally uniform, and the influence of stratospheric aerosols, which can cause increased stratospheric temperatures of 5-6 K (Guerlet et al., 2015), was not considered. Going one step further, Hue et al. (2016) coupled the radiative model of Greathouse et al. (2010) with the photochemical model of Hue et al. (2015), showing how seasonal variations of the hydrocarbons would influence the thermal field (and vice versa), but without coupling to a full dynamical model. The main effect was on the thermal field at high latitudes (Figs. 11.4 and 11.5), as seasonal chemistry and transport affects the distribution of stratospheric coolants.

Despite these differing complexities, all three models effectively reproduce the CIRS trends, once the equatorial



stratospheric oscillation is discounted, confirming the dominance of radiative heating and cooling in shaping Saturn's temperatures. At 1 mbar in Fig. 11.4, the 6-to-8-year phase lag between minimum insolation (winter) and the coolest stratospheric temperatures is correctly predicted by all of the models, reproducing the timings of temperature maxima and minima to the extent allowed by the 13-year span of the CIRS data. The results of Hue et al. (2016) suggest that this replication of the phase lags can be improved still further when the meridional and temporal variation in stratospheric coolants is also included, ideally via coupling to a circulation model, rather than holding them fixed with latitude and time. At higher altitudes (0.01 mbar) in the spring hemisphere (Fig. 11.5), radiative modelling suggests that as the insolation level increases, the stratosphere heats up with limited cooling due to the low abundances of photochemical by-products of methane at that time. Later during that season, as the amounts of  $C_2H_2$  and  $C_2H_6$  increase (see Section 11.3), the atmospheric cooling rates balance out the heating and the temperature decreases. This produces a 0.01-mbar temperature peak before the  $L_s = 270^\circ$  solstice in Fig. 11.4 at  $80^\circ S$  in Fig. 11.5 (Hue et al., 2016).

Quantitative differences in absolute temperatures between the models are likely related to the differing hydrocarbon assumptions (detailed in Section 10.2.4 of Fletcher et al., 2018b), and potentially to the absence of latitudinally- and temporally-variable aerosols. Guerlet et al. (2014) calculated that the radiative contribution from minor species such as  $C_3H_8$ ,  $CH_3C_2H$ ,  $C_4H_2$  and  $CH_3D$  would be about 5% of the total cooling rate, and therefore neglected them in their model. Inclusion of both dynamical redistribution of energy and hydrocarbons (particularly in the location of ring shadowing, Guerlet et al., 2009), alongside seasonal photochemistry and aerosols, may eventually close the gap between the models and the observations. Indeed, where cool regions under the ring's shadow were observed in the RC model of Guerlet et al. (2014), dynamical heating was produced in the GCM of Bardet et al. (2021). A similar result was obtained in the circulation model of Friedson and Moses (2012), with subsidence (of order 0.2 mm/s at 1 mbar) and warming at low latitudes in winter, removing this cold thermal anomaly. At high latitudes, Fletcher et al. (2015) suggested that vertical velocities (and thus adiabatic warming/cooling) as small as 0.1 mm/s could account for discrepancies between obser-

**Figure 11.4** Comparison of the reconstructed 1-mbar temperature field from Fig. 11.3 with simulations from Hue et al. (2016), Guerlet et al. (2014) and Friedson and Moses (2012). Only the latter model includes the influence of atmospheric circulation, but all three are successful in reproducing the seasonal asymmetries and the approximate timings of maxima and minima in temperature.

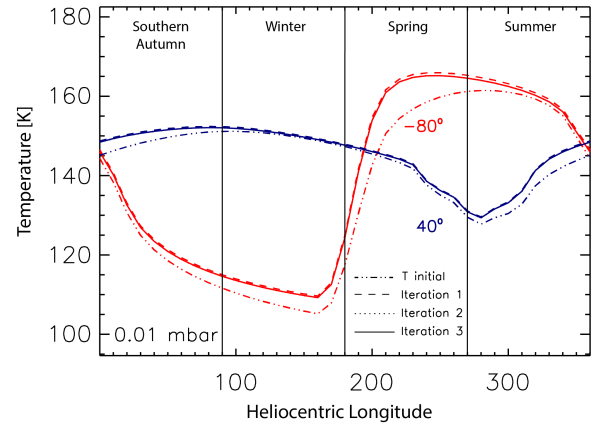


**Figure 11.5** Seasonal evolution of temperature at 0.01 mbar and latitudes of  $40^\circ N$  (blue) and  $80^\circ S$  (red). The multiple iterations between the photochemical and radiative seasonal models of Hue et al. (2016) are shown as different lines (dash double dotted line: initial state, dashed lines: first iteration, solid line: final iteration).

vations and these simple equilibrium models at the 1-mbar level.

Aerosols have a direct and measurable impact on Saturn's tropospheric temperature, producing localised heating between the radiative-convective boundary and the tropopause (sometimes referred to as the 'temperature knee') that was enhanced in southern summer, weak or absent in northern winter, and elevated over the equator (Fletcher et al., 2007; Hanel et al., 1981; Lindal et al., 1985). This localised heating was also observed in the models of Friedson and Moses (2012) and Guerlet et al. (2014), confirming it to be a radiative effect, and Guerlet et al. (2014) suggested that larger tropospheric aerosols would increase the size of the thermal perturbation. Fletcher et al. (2016) tracked the curvature of Saturn's tropospheric temperature profiles (i.e., the derivative of the lapse rate), and showed the perturbation grew

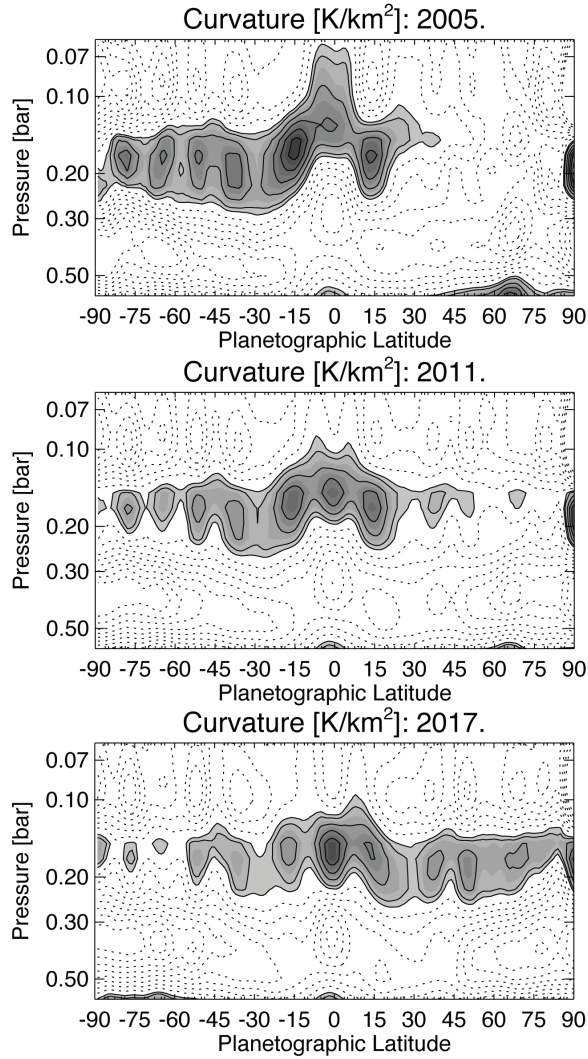


**Figure 11.6** Seasonal progression of the temperature knee from Fletcher et al. (2016), extended to 2017. The term ‘curvature’ refers to the vertical gradient of the lapse rate. Contours are spaced every  $0.004 \text{ K/km}^2$ , with grey shading and solid lines used to indicate the strongest negative curvature (i.e., the strongest temperature knee), and dotted lines showing positive curvature. The influence of the stratospheric oscillation can also be seen in the equatorial region.

smaller in the southern autumn and began to extend northwards in the spring hemisphere by 2014. Fig. 11.6 extends this analysis to the end of the Cassini mission, showing the continued growth in the springtime hemisphere due to increased insolation (Friedson and Moses, 2012) and, possibly, temporal changes in the aerosol content (Karkoschka and Tomasko, 2005).

### 11.2.2 Connecting Stratosphere and Thermosphere

*How do the mid-stratospheric temperatures connect to the thermosphere?* The shifting hemispheric contrasts and polar vortices are primarily driven by radiative balance and atmospheric circulation in the stratosphere, but here we note

potential connections to higher altitudes. At nanobar pressures, far above the stratospheric domain sensed by CIRS, exospheric temperatures increase to 400–500 K (Koskinen et al., 2015). Saturn’s main auroral ovals (Badman et al., 2011) appear to encompass the stratospheric polar vortices (Fletcher et al., 2018a), suggesting possible links between particle precipitation, energy deposition, and potentially ion-neutral chemistry at high latitudes within the polar vortices. The thermosphere is deeper at the poles, leading to substantially higher temperatures than at lower latitudes in the lower thermosphere, reminiscent of the warm vortices observed in the stratosphere. However, a pole-to-pole map of upper thermospheric temperatures from UVIS stellar occultations (Brown et al., 2020) suggests that temperatures peak near  $60\text{--}70^\circ$  latitude and then decline towards each pole. Furthermore, energy is redistributed through the thermosphere equatorward from the auroral regions, potentially due to gravity wave drag enabling meridional circulation (Brown et al., 2022). The cool poles are counter to the Saturn Thermosphere Ionosphere General Circulation Model (STIM, Müller-Wodarg et al., 2019) simulations, which suggests that the warm regions poleward of  $80^\circ$  latitude for the lower thermosphere should also persist at nanobar pressures. This discrepancy remains a topic of active research. Furthermore, the STIM model predicts warmer summertime thermospheric temperatures due to enhanced resistive (Joule) heating – this is due to larger solar ionisation and ionospheric plasma densities, rather than due to direct solar heating. However, to date the UVIS occultation data do not show evidence for seasonal asymmetries in temperature (Brown et al., 2020). This could be a consequence of the effective northward offset of Saturn’s magnetic field (Dougherty et al., 2018), with the weaker southern field producing a wider area of high Joule heating rates in the south (Müller-Wodarg et al., 2006) that balance the enhanced Joule heating in the northern summer hemisphere. Connecting these processes at nanobar pressures to millibar and microbar pressures remains a significant modelling challenge, and future progress may be made via comparison to Jupiter’s time-variable auroral heating (O’Donoghue et al., 2021), chemistry (Sinclair et al., 2019), aerosol production (Zhang et al., 2013), and high-altitude winds (Johnson et al., 2018; Cavalié et al., 2021).

Saturn’s temperatures have continued to evolve beyond northern summer solstice, and it will be the role of ground-based (Guerlet et al., 2017; Blake et al., 2022) and space-based (Norwood et al., 2016) infrared observations to extend the time series, as discussed briefly in Section 11.5.

## 11.3 Seasonal Variations in Atmospheric Composition

Whereas the seasonal changes in tropospheric and stratospheric temperatures have been straightforward to deduce from Cassini remote sensing, the changes to gaseous abundances are extremely challenging to measure due to degeneracies inherent in spectral inversions. In this section we



review changes to spatial distributions of chemicals as Saturn approached northern summer solstice, starting in the troposphere and moving into the stratosphere.

### 11.3.1 Tropospheric Composition Variations

An overview of Saturn’s tropospheric composition, including both condensation processes and photochemistry, can be found in [Fouchet et al. \(2009\)](#) and [Fletcher et al. \(2018b\)](#). Of the key volatile species ( $\text{NH}_3$ ,  $\text{H}_2\text{S}$ ,  $\text{H}_2\text{O}$ ), only ammonia has been mapped as a function of latitude, revealing contrasts between the equatorial zone and neighbouring belts indicative of equatorial upwelling ([Fletcher et al., 2011a](#); [Laraia et al., 2013](#); [Janssen et al., 2013](#); [Barstow et al., 2016](#)), and hints of a subtle north-south asymmetry (with less  $\text{NH}_3$  in the cooler northern hemisphere during winter, potentially due to condensation, [Fletcher et al., 2011a](#); [Hurley et al., 2012](#)). Of the disequilibrium ‘quenched’ species ( $\text{CO}$ ,  $\text{PH}_3$ ,  $\text{GeH}_4$ ,  $\text{AsH}_3$ ) that trace mixing from the deeper troposphere, only arsine and phosphine have been mapped with latitude, and both show moderately elevated abundances in the southern summer compared to northern winter ([Fletcher et al., 2009b, 2011a](#)). As the vertical profile of  $\text{PH}_3$  is sensitive to UV photolysis ([Kaye and Strobel, 1984](#); [Visscher et al., 2009](#)), this may be evidence of UV shielding by increased aerosol opacity in the southern summer hemisphere ([Fletcher et al., 2018b](#)), although we caution that abundances extracted from VIMS  $5\text{-}\mu\text{m}$  observations are somewhat degenerate with the assumed aerosol properties. To date, no seasonal studies of  $\text{NH}_3$ ,  $\text{PH}_3$ , or  $\text{AsH}_3$  have been performed, and models that predict the seasonal variation of tropospheric photochemistry on Saturn have not yet been developed. The question of whether the subtle asymmetries are permanent or time-variable remains unanswered, and the feedback effects of aerosol- and self-shielding (i.e., reducing the rates of photolytic destruction) remain unexplored. We discuss changes in the high-latitude distribution of  $\text{PH}_3$ , and the putative diphosphine ( $\text{P}_2\text{H}_4$ ) layer, in Section 11.4.

More progress has been made in the study of Saturn’s para-hydrogen distribution, which traces both mixing from the deeper troposphere and the efficiency of interconversion between spin isomers of  $\text{H}_2$  (catalysed by the presence of paramagnetic sites on aerosols with equilibration timescales of 90-160 years at 200 mbar, [Fouchet et al., 2003](#)). The shape of the far-infrared collision-induced continuum is determined by the ratio of ortho- $\text{H}_2$  (odd rotational spin isomer with parallel spins governing the broad  $\text{S}(1)$  feature near  $587\text{ cm}^{-1}$ ) and para- $\text{H}_2$  (even spin isomer with anti-parallel spins governing the broad  $\text{S}(0)$  feature near  $354\text{ cm}^{-1}$ ) ([Massie and Huntten, 1982](#)). At high temperatures in the deeper troposphere, the fraction of para- $\text{H}_2$  ( $f_p$ ) makes up 25% of the molecular hydrogen, whereas the equilibrium fraction increases to 45-50% at the cold tropopause. Displacement of air parcels from the deeper troposphere at a rate faster than the ortho-to-para conversion means that the low para- $\text{H}_2$  fraction is ‘frozen in’. These ‘sub-equilibrium’ conditions indicate uplift from deeper, warmer levels, which seems to be the case at the equator ([Fletcher et al., 2007, 2016](#)) and at the latitudes of Saturn’s 2010-11

northern storm ([Achterberg et al., 2014](#)). Conversely, ‘super-equilibrium’ can indicate sinking from higher, cooler altitudes near the tropopause. The extent of this disequilibrium is seasonal: [Conrath et al. \(1998\)](#) reported super-equilibrium conditions and higher  $f_p$  in the springtime hemisphere ( $30^\circ\text{S}$  to  $70^\circ\text{N}$ ) during the Voyager era, [Fletcher et al. \(2007\)](#) showed that this had reversed by southern summer observed by Cassini, with sub-equilibrium in the winter hemisphere polewards of  $30^\circ\text{N}$ . [Fletcher et al. \(2016\)](#) showed that super-equilibrium conditions moved northwards as winter turned to spring (see Fig. 11.7c, right), and sub-equilibrium conditions emerged in southern autumn. Although small changes in  $f_p$  were occurring, much of this asymmetry in disequilibrium can be simply attributed to changing temperatures (and thus the change in the equilibrium para- $\text{H}_2$  fraction), without invoking large-scale circulation or changes in aerosol catalysis.

In Fig. 11.7 we extend the  $f_p$  mapping from far-IR inversions ([Fletcher et al., 2016](#)) to 2017. This confirms that  $f_p$  was relatively stable with time at 220 mbar, and shows the increase in  $f_p$  in the northern hemisphere throughout the mission ([Fletcher et al., 2016](#)), only perturbed in the  $15 - 45^\circ\text{N}$  range by the low- $f_p$  air brought upwards by the 2010-11 storm. At 440 mbar  $f_p$  showed an asymmetry pre-equinox with lower  $f_p$  in the summer hemisphere than in the winter. A similar asymmetry was observed by Voyager in early northern spring ([Conrath et al., 1998](#); [Fletcher et al., 2016](#)). CIRS results in Fig. 11.7b reveal that this asymmetry begins to reverse and become more symmetric after equinox as  $f_p$  increased faster in the mid-to-high southern latitudes than anywhere else, although this interpretation is significantly complicated by the influence of the 2010-11 storm. This can be compared to the expectations for an inter-hemispheric meridional circulation at Saturn ([Conrath et al., 1990](#)) — a two-cell circulation pattern near equinox would lead to subsidence at high latitudes in both hemispheres (their Fig. 10), but approaching solstice the subsidence in the southern winter hemisphere would be stronger (their Fig. 9), rapidly increasing  $f_p$  in the south. With the demise of Cassini, continued monitoring of Saturn’s para- $\text{H}_2$  will be challenging — will it continue to exhibit latitudinal asymmetries as indirect evidence of seasonally changing interhemispheric circulation? The spatial distribution of  $f_p$  in the stratosphere remains completely unknown. Furthermore, there is currently no predictive seasonal model that combines the effects of meridional circulation, local dynamical mixing (e.g., at the equator), and the catalytic effects of aerosols on the conversion between ortho- and para- $\text{H}_2$ .

### 11.3.2 Stratospheric Composition Variations

The photolysis of methane in Saturn’s upper stratosphere gives rise to a complex network of hydrocarbon species, including  $\text{C}_2$  species (ethane, acetylene, ethylene),  $\text{C}_3$  species (propane, methylacetylene) and higher-order hydrocarbons (diacetylene, benzene, etc.). The photochemical reactions responsible for producing these species were reviewed previously ([Fouchet et al., 2009](#); [Fletcher et al., 2018b](#)), alongside the published measurements of hydrocarbon abun-



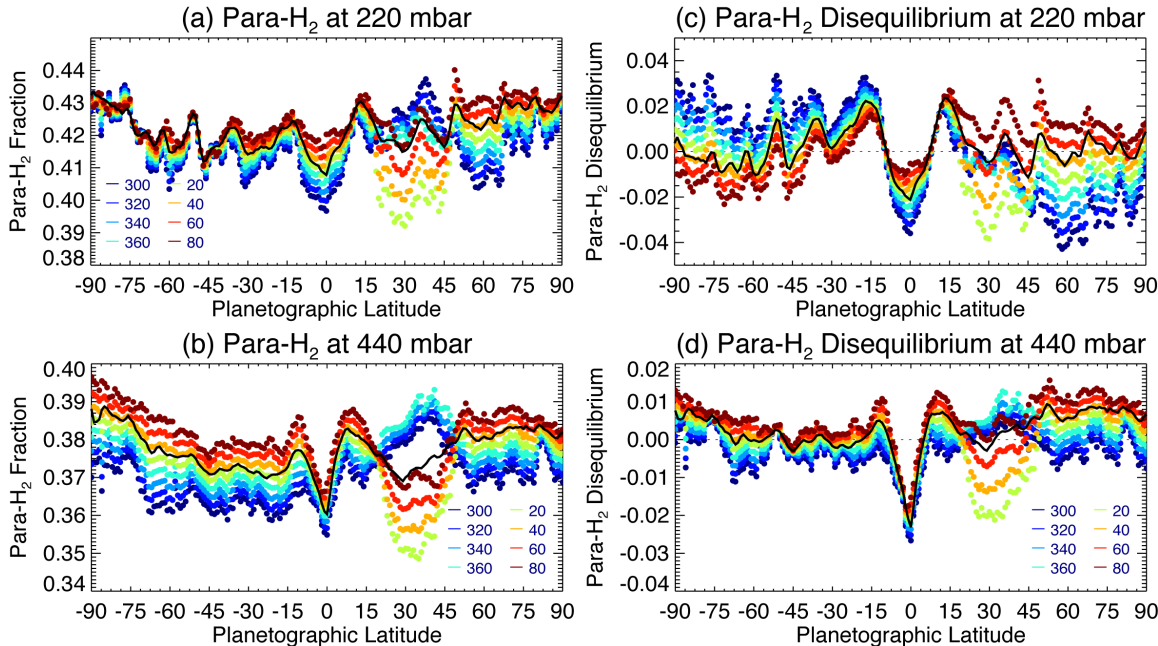


**Figure 11.7** Latitudinal distribution of para- $\text{H}_2$  fraction (left) and extent of disequilibrium (right) at 220 and 440 mbar, updated from Fletcher et al. (2016). Distributions at different values of  $L_s$  are extracted from a linear interpolation to the full CIRS time series, with a two-step linear fit used for latitudes perturbed by the 2010-11 northern storm (Achterberg et al., 2014). Solid black lines represent the mean of all inversions during the 13-year mission. Dotted horizontal black lines in the disequilibrium plots denote equilibrium conditions. Typical uncertainties on  $f_p$  inversions are  $\sim \pm 0.01$  (Fletcher et al., 2016).

dances from Voyager, Cassini, and ground-based observations before 2014. Cassini's contribution was to measure the latitudinal distributions of stratospheric species at various points during the 2004-2017 time series. CIRS observations of ethane ( $\text{C}_2\text{H}_6$ ) and acetylene ( $\text{C}_2\text{H}_2$ ) have been sufficient to trace seasonal evolution (Howett et al., 2005; Hesman et al., 2009; Guerlet et al., 2009, 2010; Sinclair et al., 2013, 2014; Sylvestre et al., 2015; Fletcher et al., 2015, 2018a), but before we discuss those findings, we briefly mention the observed distributions of the higher-order hydrocarbon species.

Propane ( $\text{C}_3\text{H}_8$ ) at 1 mbar appears to track the instantaneous solar insolation (Guerlet et al., 2009), but no changes were observed between 2005-06 and 2010 (Sylvestre et al., 2015). Ethylene ( $\text{C}_2\text{H}_4$ ) has only been observed in the warm-temperature aftermath of the 2010-11 storm (Hesman et al., 2012; Moses et al., 2015), and its latitudinal distribution remains unknown. Methylacetylene ( $\text{C}_3\text{H}_4$ ) and diacetylene ( $\text{C}_4\text{H}_2$ ) were depleted in southern summer mid-latitudes compared to northern winter mid-latitudes, potentially indicating stratospheric upwelling of hydrocarbon-poor air during the southern summer and subsidence of hydrocarbon-rich air in northern winter (Guerlet et al., 2010). Benzene ( $\text{C}_6\text{H}_6$ ), measured by both CIRS limb measurements (Guerlet et al., 2015) and UVIS stellar occultations (Koskinen et al., 2016), appears to be at least as abundant at the southern summer pole compared to the equator, suggesting a role for ion-neutral chemistry in producing benzene at high latitudes (see Section 11.3.3). At the time of writing, work continues to study the temporal variability of these species as Saturn approached northern summer solstice.

We therefore focus this section on new results on ethane and acetylene spanning the duration of Cassini's mission, as shown in Fig. 11.8. Both Guerlet et al. (2009) and Sylvestre et al. (2015) utilised the enhanced vertical resolution of

CIRS limb-sounding to measure the vertical distributions in the 0.01-5.0 mbar range, enabling a comparison of pre-equinox (2005-2008) and post-equinox (2010) observations, and both datasets are shown as squares in Fig. 11.8. These are compared to crude estimates of ethane and acetylene distributions from CIRS nadir observations at low spectral resolution ( $15 \text{ cm}^{-1}$ ) but high temporal resolution. Snapshots of these observations were presented by Sinclair et al. (2013, 2014), but individual spectral inversions are sensitive to calibration defects and extreme degeneracies with the determination of stratospheric temperatures. In Fig. 11.8 we adopt the technique of Fletcher et al. (2017) and Fletcher et al. (2018a), fitting tensioned splines as a function of time at each latitude to remove significant outliers and extract general trends. The caveat is that any short-term variability (on the order of months) would be smoothed over, and that the 2011-2013 period perturbed by Saturn's northern storm had to be removed from the time series. Polar results were previously shown by Fletcher et al. (2018a), and the figures are extended here to cover all latitudes. We caution the reader that nadir observations have limited sensitivity to the 0.1-mbar level, and so do not show the same large-scale variability as the limb measurements.

The nadir time series is also shown in Fig. 11.9 for the 1-mbar altitude, and is compared to the seasonal predictions

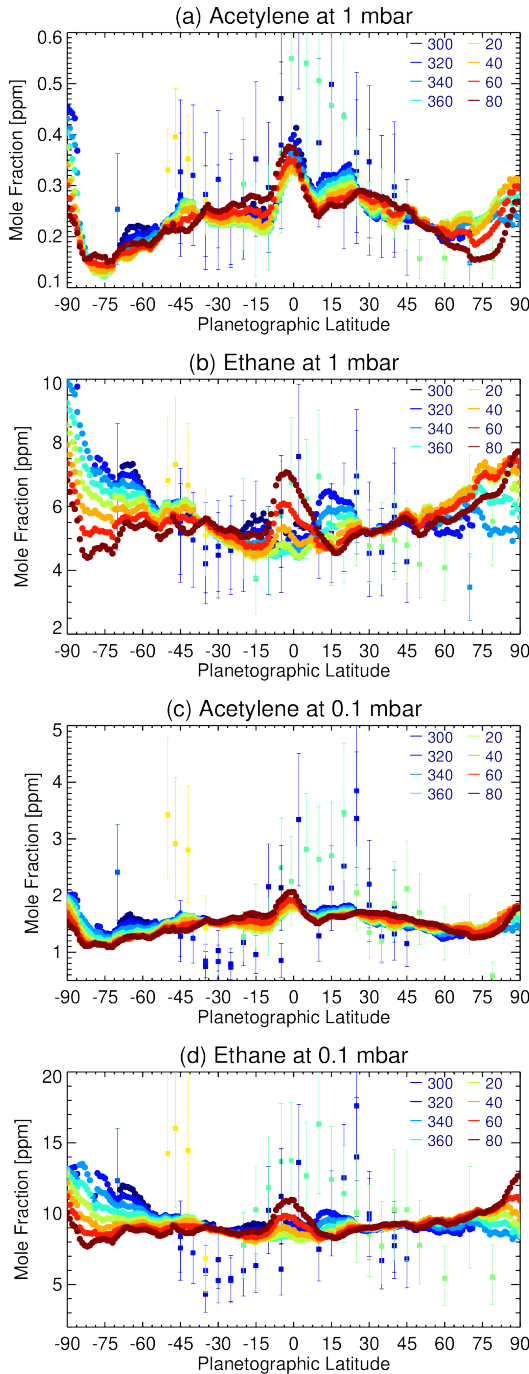


**Figure 11.8** Cassini CIRS nadir and limb results for acetylene and ethane at 1 mbar and 0.1 mbar, adapted from [Fletcher et al. \(2018a\)](#) (nadir results as circles, reconstructed from smooth spline fits to inversions of  $15\text{-cm}^{-1}$  resolution spectra and extended to all latitudes), [Guerlet et al. \(2009\)](#) (limb results in 2005–08 as blue-green squares before  $L_s = 360^\circ$ ) and [Sylvestre et al. \(2015\)](#) (limb results in 2010–12 as yellow-orange squares after  $L_s = 360^\circ$ ). Note that nadir data do not have sensitivity to the 0.1-mbar level, which is why latitudinal contrasts are much smaller than those observed in the limb data - the observed nadir structure represents the influence of information content in the 0.5–1.0 mbar level and smoothing to lower pressures. Furthermore, nadir retrievals cannot fully capture the oscillatory structure of Saturn’s equatorial temperature profile, so low-latitude hydrocarbon distributions should be treated with caution. The colours correspond to different  $L_s$ , as labelled.

of [Hue et al. \(2015\)](#) and [Moses and Greathouse \(2005\)](#), discussed below. Several features of the latitudinal distributions stand out:

- The  $\text{C}_2\text{H}_2$  distribution at 0.1 and 1 mbar shows a strong decline from the equator to  $\sim 70^\circ$  latitude in both hemispheres, tracking the annual-average insolation, whereas the  $\text{C}_2\text{H}_6$  is more latitudinally uniform with a rise towards high latitudes. A similar situation occurs on Jupiter ([Hue et al., 2018](#)), and to date, there is no chemical explanation for the difference between these two species, which are expected to be coupled and to both show similar equator-to-pole gradients (Fig. 11.9).
- By summer solstice, both species show an equatorial maximum in abundance within  $\pm 10^\circ$  latitude, but the local equatorial peak in the  $\text{C}_2\text{H}_6$  distribution developed only after 2012, possibly in association with Saturn’s Equatorial Stratospheric Oscillation. The  $\text{C}_2\text{H}_2$  maximum appears relatively stable over the course of the dataset. However, these nadir retrievals cannot resolve the vertical temperature structure associated with Saturn’s equatorial oscillation ([Fouchet et al., 2008](#)), so the equatorial hydrocarbon results within  $\pm 10^\circ$  should be treated with caution.
- There are hints of complex temporal variability in the  $10 - 25^\circ$  latitude ranges in both hemispheres, but more pronounced in the north. The seasonally-reversing Hadley cell of [Friedson and Moses \(2012\)](#) predicts subsidence of hydrocarbon-rich air near  $25^\circ$  in the winter hemisphere, consistent with the local maximum in the  $10 - 25^\circ\text{N}$  region in Fig. 11.8 for ethane and acetylene. This winter subsidence appears to weaken at 1 mbar over time (comparing  $L_s = 308^\circ$  to  $L_s = 134^\circ$  in [Friedson and Moses, 2012](#)), with diffusion helping to remove the local maximum in the later nadir and limb data by the spring ([Sylvestre et al., 2015](#)). The effects of Saturn’s ring shadow ([Guerlet et al., 2009](#)), and the downward propagation of the extratropical features of Saturn’s Equatorial Stratospheric Oscillation ([Fletcher et al., 2017](#)), may also be playing a role at these latitudes.
- Limited seasonal change is apparent at Saturn’s mid-latitudes in Fig. 11.8, in partial disagreement with earlier results ([Sinclair et al., 2013](#)).
- Conversely, the largest changes are occurring within the Northern and Southern Polar Stratospheric Vortices (NPSV and SPSV, [Fletcher et al., 2018a](#)), with declining abundances at the south pole (potentially due to upwelling of hydrocarbon-poor air in southern autumn) and increasing abundances at the north pole (potentially due to subsidence of hydrocarbon-rich air in northern spring), or with as-yet-undetermined auroral influences on polar chemistry.

Another important result from Cassini/CIRS was to show that seasonal variations of stratospheric composition are more muted than initially predicted. Although the 1-mbar trends are expected to be small, one-dimensional photochemical models at lower pressures predicted seasonal abundance variations up to a factor of 10 at 0.01 mbar and high latitudes for  $\text{C}_2\text{H}_2$  ([Moses and Greathouse, 2005](#); [Hue et al., 2015](#)). Despite the limited temporal coverage of limb ob-

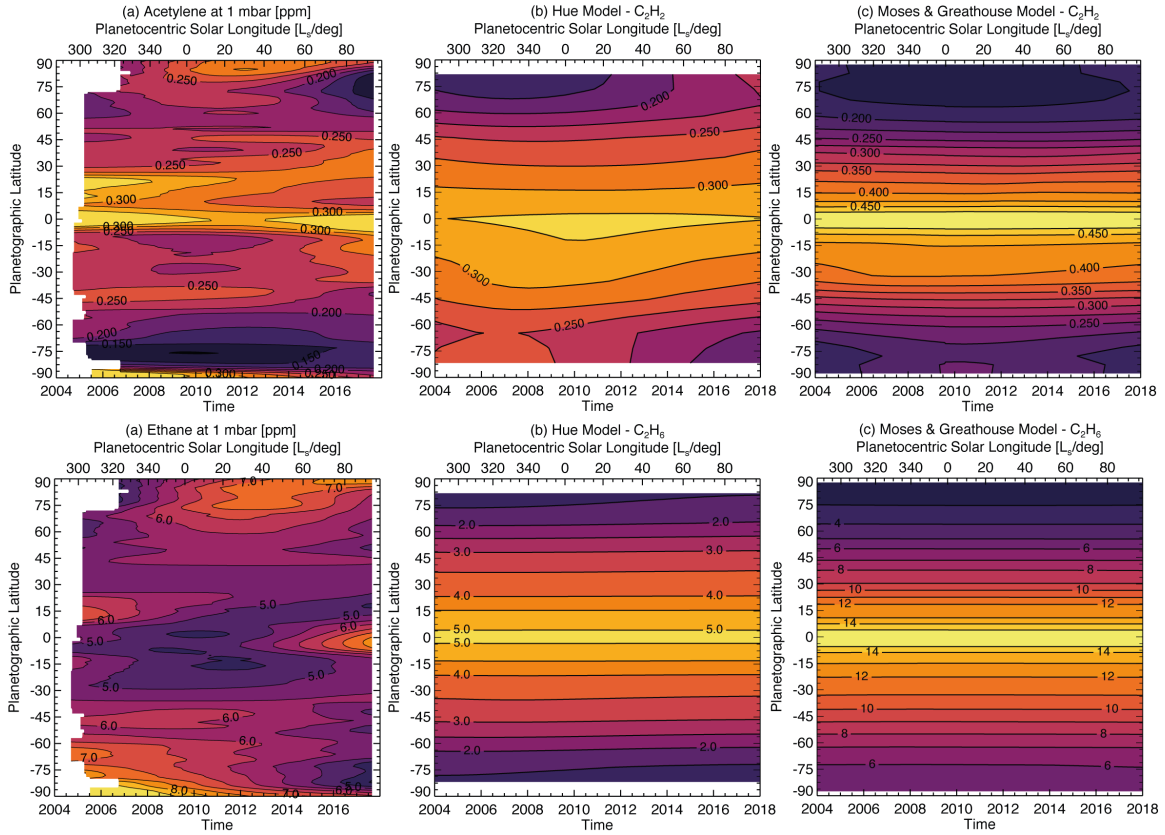


**Figure 11.9** Reconstructed mole fractions for ethane and acetylene at 1 mbar. Left-hand column shows abundances from CIRS nadir observations, constructed by fitting tensioned splines through the time series of retrievals at each latitude as described by [Fletcher et al. \(2018a\)](#). Variability smaller than the difference between contour levels (i.e., smaller than 0.05 ppm for  $C_2H_2$ , or 1 ppm for  $C_2H_6$ ) is likely due to uncertainties in the spectral inversion. Central and right column show predicted abundances based on the photochemical modelling of [Hue et al. \(2015\)](#) and [Moses and Greathouse \(2005\)](#) over the 2004–2018 time span of the Cassini mission, highlighting the discrepancy between data and models.

servations over one season ( $\Delta L_s \sim 90^\circ$ ), such large-scale changes have not been observed. The absence of such strong contrasts may imply that meridional transport is an efficient process that redistributes the seasonally-produced hydrocarbons. The discussion above hints at a complex balance between photochemistry and atmospheric circulation, discussed in the next section.

### 11.3.3 Stratospheric Chemistry Modelling

Proper modelling of the stratospheric physico-chemistry implies coupling a general circulation model that calculates the spatio-temporal distribution of several tens of compounds while simultaneously accounting for (photo-)chemical reactions. This is an especially computationally demanding task since the production of higher-order hydrocarbons, and the subsequent formation of hazes and aerosols, implies hundreds of chemical reactions (e.g., [Wong et al., 2000, 2003](#), for Jupiter). Furthermore, uncertainties in the chemical reaction rates have to be considered, as they affect the accuracy of photochemical model predictions ([Dobrijevic et al., 2003](#)), particularly for the higher-order hydrocarbons. Reduced chemical networks allow computing the abundances of a smaller subset of compounds with great fidelity while limiting the computational cost ([Dobrijevic et al., 2011](#)).

No models have yet succeeded at self-consistently accounting for that coupling, although different approaches have been taken in that direction. [Friedson and Moses \(2012\)](#); [Greathouse et al. \(2010\)](#); [Dowling et al. \(2010\)](#); [Guerlet et al. \(2014\)](#); [Spiga et al. \(2020\)](#) developed general circu-

lation models that include the effect of heating and cooling from the main stratospheric compounds but, as described in Section 11.2, the spatial distributions of the main coolants (i.e.,  $C_2H_2$  and  $C_2H_6$ ) are assumed to stay constant in time, counter to the changes observed in Fig. 11.8. Conversely, photochemical models generally use a pseudo-2D (altitude-latitude) approach, either by modelling a sum of 1D vertical columns at different latitudes ([Moses and Greathouse, 2005](#)), or as a 2D-model without meridional transport ([Hue et al., 2015](#)), equivalent to a 1D approach. Atmospheric circulation is neglected in these photochemical models for Saturn, but there have been attempts to couple photochemistry and transport for Jupiter ([Hue et al., 2018](#)). In our previous review ([Fletcher et al., 2018b](#)), we presented a comparison between the photochemical predictions of [Moses and Greathouse \(2005\)](#) and the hydrocarbon abundances recorded in the CIRS nadir and limb observations. In Fig. 11.9 we therefore restrict the comparison to ethane and acetylene at 1 mbar, considering the model of

Hue et al. (2016) which includes feedback between the temperature and abundance fields as explained in Section 11.2. The key conclusion from Fig. 11.9 is that the hydrocarbon observations suggest a more complex behaviour than the models can currently account for.

One-dimensional fixed-season photochemical models have also been developed to explain the observed abundances of  $\text{CH}_4$ ,  $\text{C}_2\text{H}_2$ ,  $\text{C}_2\text{H}_4$ ,  $\text{C}_2\text{H}_6$ , and  $\text{C}_6\text{H}_6$  in the stratospheric homopause region of Saturn, as retrieved from the *Cassini* UVIS occultations (Koskinen et al., 2016). These models focused on specific latitudes and seasons relevant to the UVIS occultations, and the results indicated that neutral photochemistry alone was insufficient to explain the observed hydrocarbon abundances, particularly with respect to benzene. An extra hydrocarbon production source is needed in the upper stratosphere, suggested to be ion-neutral chemistry initiated by either absorption of solar extreme ultraviolet radiation (which has a seasonal dependence), or by interaction of magnetospheric charged particles with the atmosphere in the auroral regions (which has a latitude dependence), or a combination of the two. The fact that the benzene mixing ratio is observed to be more than an order of magnitude greater at high northern latitudes in spring, in comparison with similar high southern latitudes in late autumn after this region entered the perpetual darkness of polar winter, has prompted Koskinen et al. (2016) to conclude that solar-driven ion chemistry plays an important role in  $\text{C}_6\text{H}_6$  production — auroral chemistry alone and subsequent transport away from the auroral regions is not the sole mechanism for producing and distributing benzene on Saturn.

Further ion-neutral photochemical modelling by Moses et al. (2018) confirmed the conclusions of Koskinen et al. (2016) in that solar-UV driven ion chemistry results in a factor of  $<\sim 10$  increase in the abundance of benzene and polycyclic aromatic hydrocarbons (PAHs) in comparison with models that consider neutral chemistry alone; however, the models also show that ion chemistry has less of an influence on the abundance of smaller  $\text{C}_2\text{H}_x$  hydrocarbons. Moses et al. (2018) determined that solar-driven ion chemistry leads to a strong seasonal dependence of the benzene production rate, with more  $\text{C}_6\text{H}_6$  being produced in summer than winter. These models, which include solar chemistry but no auroral chemistry, underpredict the abundance of neutral hydrocarbon photochemical products at the high stratospheric altitudes probed by UVIS at high latitudes near the auroral regions. As discussed by Moses et al. (2018), auroral ion chemistry could potentially make up some of this shortfall but is unlikely to fully resolve the model-data mismatch, suggesting that atmospheric dynamics could be affecting high-altitude species' distributions on Saturn.

Recent non-seasonally-dependent chemical models have confirmed the influence of exogenic material on Saturn's stratospheric chemistry. Oxygen and other elements can be delivered via cometary impacts, interplanetary dust particles, or local satellite/ring sources, with  $\text{H}_2\text{O}$ ,  $\text{CO}$ , and  $\text{CO}_2$  becoming the dominant stable products from oxygen chemistry (Moses and Poppe, 2017). From models of dust-particle dynamics in the outer solar system, and models of

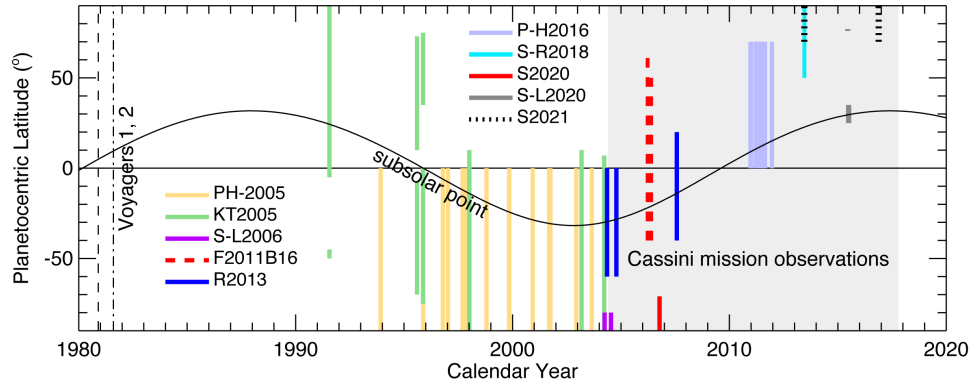
dust ablation and subsequent stratospheric photochemistry in Saturn's atmosphere, Poppe (2016) and Moses and Poppe (2017) concluded that the influx of interplanetary dust particles was insufficient to explain the relatively large abundance of  $\text{H}_2\text{O}$ ,  $\text{CO}$ , and  $\text{CO}_2$  in Saturn's stratosphere (e.g., Feuchtgruber et al., 1997). Ever since active plumes were discovered on Enceladus by Cassini (Dougherty et al., 2006; Porco et al., 2006), this icy moon has been suggested as the dominant source for Saturn's stratospheric water (e.g., Guerlet et al., 2010; Cassidy and Johnson, 2010; Hartogh et al., 2011; Fleshman et al., 2012), and spatially resolved stratospheric  $\text{H}_2\text{O}$  observations by Herschel have validated this conclusion (Cavalié et al., 2019). Saturn's stratospheric  $\text{CO}$ , on the other hand, may result from a large cometary impact that occurred several hundred years ago (Cavalié et al., 2010; Moses and Poppe, 2017). The large influx of ring vapour observed to be entering Saturn's upper atmosphere from *in situ* measurements during the Grand Finale stage of the Cassini mission (Waite et al., 2018; Miller et al., 2020; Serigano et al., 2022) is also expected to affect Saturn's stratospheric chemistry (Moses et al., 2023). However, the expected chemical consequences were not seen by contemporaneous Cassini UVIS or CIRS observations, suggesting that the inferred large ring-vapour influx derived from a recent dynamical event in the rings (see, e.g., Hedman, 2019), or that most of the ring material enters the atmosphere as small dust particles that never actually ablate and therefore do not significantly affect stratospheric chemistry (see Moses et al., 2023). Chapters by Koskinen et al. and Moore et al. in this volume provide more detail on the effects of external material on Saturn's thermosphere and ionosphere.

In summary, Cassini has revealed slow seasonal changes in the distributions of  $\text{C}_2\text{H}_x$  species over half a Saturnian year, as well as hemispheric asymmetries in other molecules, but these are yet to be fully explained by coupled neutral chemistry, ion chemistry, and atmospheric circulation models. Continued tracking of spatio-temporal changes, alongside future model development, are needed to understand Saturn's seasonal variability.

## 11.4 Aerosol Variability

At the time of the previous overview of our understanding of Saturn's aerosols by Fletcher et al. (2018b), there was a consensus that seasonal insolation changes induce hemispheric asymmetries in the tropospheric (and likely stratospheric) hazes, with higher opacity in the summer hemisphere and lower opacity and a bluer visual colour in the winter hemisphere. Consistent asymmetries were also observed at near-IR wavelengths, with increased upper tropospheric opacity producing greater attenuation of Saturn's  $5\text{-}\mu\text{m}$  emission in the summer hemisphere (Baines et al., 2006; Fletcher et al., 2011a). There was also a consensus that upper tropospheric aerosols reach to higher altitudes at the equator and stratospheric aerosols reach their greatest opacity in the polar regions. As Saturn proceeded through its seasonal changes over the last 40 years, there has been





an evolution in instrumental capabilities and observational constraints that enables a more discriminating investigation of Saturn's aerosols, which we focus on in this improved but still incomplete assessment of seasonal aerosol variability.

#### 11.4.1 Cassini Observational Improvements in Context

Observations by Pioneer 11 in 1979, and Voyager 1 and 2 in 1980 and 1981, were limited in their spectral discrimination of vertical aerosol structure due to the use of broadband filters, yet they made important discoveries that are reviewed by West et al. (2009) and more recently and more briefly by Fletcher et al. (2018b). Here we focus on the analysis of observations by the Hubble Space Telescope (HST) between 1991 and 2004, and Cassini observations between 2004 and 2017. The temporal and latitudinal coverage of a number of key investigations using these observations are displayed in Fig. 11.10.

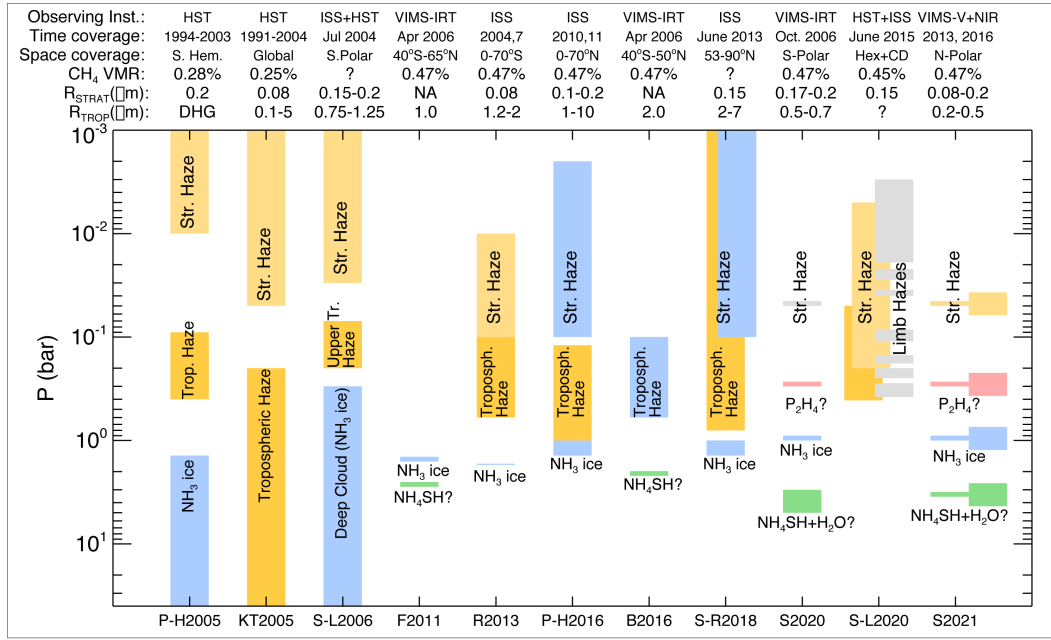
Relative to Voyager and Pioneer, HST observations provided more broadband and important narrow-band filters and sensitivity to methane band absorptions of different strengths, but were limited to low phase angles. Capabilities to constrain vertical structure were improved significantly by Cassini. Its Imaging Science Subsystem (ISS) provided better sampling of methane band absorptions at CCD wavelengths, with greatly enhanced spatial resolution and phase angle coverage relative to HST observations. Even more significant to aerosol investigations were observations by its Visual and Infrared Mapping Spectrometer (VIMS), an imaging spectrometer that covered wavelengths from 0.35 to 5.12  $\mu\text{m}$ . Along with this greater range of wavelengths, VIMS provided a wider variety of methane absorption strengths, and access to thermal emissions by Saturn, the combination of which facilitated the probing of deeper cloud structures, identification of cloud compositions, and constraining the spatial variability of phosphine gas ( $\text{PH}_3$ ). While the seasonal range of HST and Cassini observations offers great potential to characterise and understand seasonal variability in Saturn's aerosols, a comprehensive analysis including the full range of the spectral constraints offered by Cassini remains to be accomplished. Recent efforts have focused on storms (Oliva et al., 2016; Sromovsky et al., 2013, 2016, 2018) and polar regions (Sánchez-Lavega et al., 2006; Sanz-Requena

**Figure 11.10** Sub-solar latitude as a function of time, with temporal latitudinal sampling by published investigations of Saturn's aerosol distributions indicated by coloured bars for references indicated in the legend, which are Pérez-Hoyos et al. (2005), Karkoschka and Tomasko (2005), Sánchez-Lavega et al. (2006), Fletcher et al. (2011a) and Barstow et al. (2016) (combined as by F2011B16), Roman et al. (2013), Pérez-Hoyos et al. (2016), Sanz-Requena et al. (2018), Sromovsky et al. (2020b), Sánchez-Lavega et al. (2020), and Sromovsky et al. (2021). Year labels are centred on tick marks placed at the beginning of the labelled year. These do not include storm-focused publications covering small local regions.

et al., 2018; Sánchez-Lavega et al., 2020; Sromovsky et al., 2020a,b, 2021), with limited latitudinal and temporal sampling, and only one Cassini study (Sromovsky et al., 2021) has combined both simultaneous coincident visual and near-IR constraints, using both reflected sunlight and thermal emission to constrain aerosol structure models in the north polar region.

#### 11.4.2 Aerosol Vertical Structure and Composition

Aerosol vertical structure models from the publications identified in Fig. 11.10, are crudely summarised in Fig. 11.11. Vertical structure results published prior to 2006 are skewed to some degree by the assumption of a methane volume mixing ratio of 0.28%-0.25%, which is well below the currently accepted value of 0.47% (Fletcher et al., 2009a). The visual and CCD observations were generally well matched by aerosol models that included two vertically extended particle layers (note that the use of semi-infinite layers in HST-based models is only a modelling convenience that is inconsistent with near-IR observations, because they would block Saturn's 5- $\mu\text{m}$  thermal emission). The top layer in these models is a stratospheric haze of particles generally assumed to be spherical with radii of 0.1-0.2  $\mu\text{m}$ , usually distributed between 10 mbar and 100 mbar. The second layer, termed tropospheric or upper tropospheric, consists of generally larger particles, with widely varying radii from 0.1  $\mu\text{m}$  to 10  $\mu\text{m}$ , depending on time, latitude, and model assumptions, with a vertical distribution also variable, but generally distributed between 100 mbar and 1 bar. This layer has an unknown composition, with diphosphine ( $\text{P}_2\text{H}_4$ ) being the leading contender on photochemical grounds (Fouchet et al., 2009). It is definitely not primarily ammonia ice because it lacks ammonia's 3- $\mu\text{m}$  absorption signature, as inferred by



Kerola et al. (1997) from ground-based observations, and by Sromovsky et al. (2013) from VIMS near-IR observations. An alternative interpretation that the top layer might be primarily ammonia ice, but coated with other substances that obscure the ammonia spectral signatures, are less plausible because coatings do not hide those signatures very well unless they represent a significant fraction of the particle's mass (West et al., 1989).

#### 11.4.3 Revealing the Ammonia Layer

Many models illustrated in Fig. 11.11 include a deeper cloud layer assumed to be ammonia ice and placed near the pressure predicted by equilibrium cloud condensation models (ECCM) (Atreya and Wong, 2005), with a nominal cloud base at 1.7 bars. But this layer is difficult to constrain within the CCD spectral band, except for some discrete features of unusually high opacity (Roman et al., 2013). To actually identify ammonia ice, which was initially expected to be the main constituent of the uppermost cloud layer on Saturn, requires detection of its strong 3- $\mu$ m absorption feature and even better would be the additional detection of its much weaker 2- $\mu$ m absorption feature. The VIMS near-IR spectrometer has the capability to make those detections, but the appearance of that spectral signature on Saturn has been extremely rare. Until recently, ammonia ice has only been spectrally detected in the Great Storm of 2010–2011 (Sromovsky et al., 2013), and in Storm Alley (Sromovsky et al., 2018), likely because vertical convection (strongly suggested by associated lightning, Dyudina et al., 2007; Dyudina et al., 2013) had apparently elevated deeper condensates to the visible cloud level, or very near to that level in the Storm Alley case. Additional examples were subsequently found in both polar regions (Baines et al., 2018; Sromovsky et al., 2020b, 2021) where the overlying putative diphosphine layer was

**Figure 11.11** Schematic models of vertical aerosol structures used to fit observations characterised in the legend table above each reference column. Note that successful models vary greatly in assumed vertical distributions. Reference labels are the same as in Fig. 11.10. Note the multiple compact layers detected by limb observations analysed by Sánchez-Lavega et al. (2020). The yellow-orange colours mark layers with assumed or derived short wavelength absorption (the chromophore layers), with two shades used if different chromophore models are used in different layers. Stratospheric layers without shortwave absorption model fits are indicated in grey. Blue denotes NH<sub>3</sub> ice particle layers, pink possible P<sub>2</sub>H<sub>4</sub>, and green possible NH<sub>4</sub>SH or H<sub>2</sub>O ice particles. ECCM models, e.g. Atreya and Wong (2005), predict an ammonia ice layer, and an NH<sub>4</sub>SH layer with possible overlap of an even deeper water cloud. But ammonia gas depletion by the formation of the NH<sub>4</sub>SH can alter the ammonia condensation level. The stratospheric and putative P<sub>2</sub>H<sub>4</sub> layers are expected to originate from photochemistry.

found to be sufficiently transparent that the ammonia ice layer is not entirely obscured by it.

The fact that the vertical location of this third layer is in a pressure-temperature range where NH<sub>3</sub> condensation is expected, and the fact that it displays the strong 3- $\mu$ m absorption signature of ammonia, together argue that this layer is indeed primarily composed of NH<sub>3</sub> ice. One of the clearest examples of this detection is displayed in Fig. 11.12, from an investigation of Saturn's north polar eye by Baines et al. (2018). Note the ratios of reflectivity at 2.7  $\mu$ m to that at 3.1  $\mu$ m, which is about 2:1 for the background cloud spectrum in panel C, but more than 10:1 for the bright cloud spectrum in panel B. Note also that the ratio of reflectivity at 1.9  $\mu$ m to that at 2  $\mu$ m also is larger, but by smaller degrees, for clouds with increased 3- $\mu$ m absorption. The bright cloud features in panel F (a 1.29- $\mu$ m image) are also bright at 4.09  $\mu$ m, which makes them appear as magenta in the panel A colour composite because they lack reflectivity at

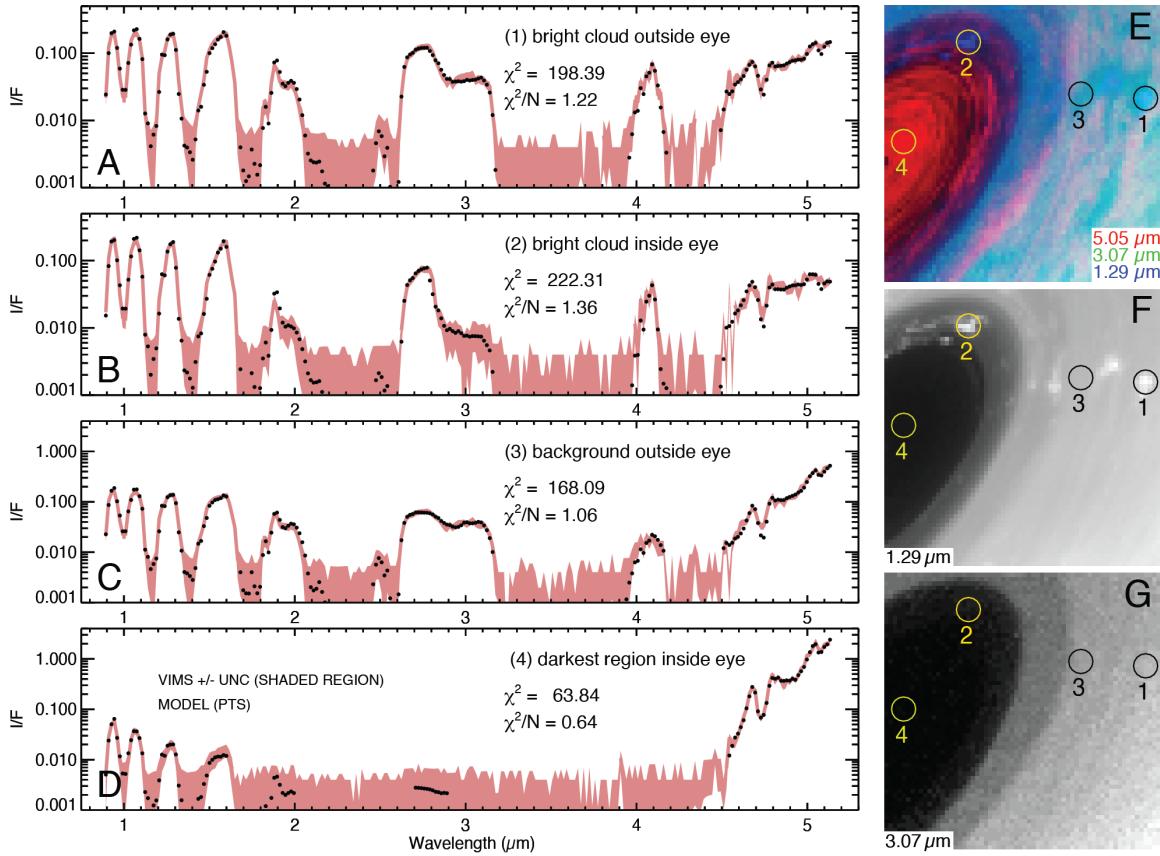


**Figure 11.12** VIMS near-IR observations of Saturn's north polar eye on 26 April 2017. Discrete bright features at 1.29 and 5.05  $\mu\text{m}$  exhibit strong absorption at 3.07  $\mu\text{m}$  due to the presence of large ammonia ice particles. Adapted from [Baines et al. \(2018\)](#).

3.07  $\mu\text{m}$ , shown in panel G. The high I/F at 4–4.1  $\mu\text{m}$  also suggests that  $\text{NH}_4\text{SH}$  is unlikely to be the main component of this 3- $\mu\text{m}$  absorbing cloud.

#### 11.4.4 Sounding the Deep Putative $\text{NH}_4\text{SH}$ Cloud

A layer of absorbing particulates in the 2–5 bar region is clearly required to modulate Saturn's 5- $\mu\text{m}$  thermal emission. Plausible constituents are  $\text{NH}_4\text{SH}$  and water ice according to ECCM predictions ([Atreya and Wong, 2005](#)), but neither species provides an accurate spectral fit alone ([Barstow et al., 2016](#); [Sromovsky et al., 2020b, 2021](#)). While  $\text{NH}_4\text{SH}$  provides better model fits, a mixed composition seems likely. While Saturn's 5- $\mu\text{m}$  emission seems to have a seasonal variation, indicated by its VIMS-observed hemispheric asymmetry in 2006 ([West et al., 2009](#)), the deep layer itself provides no evidence of significant seasonal variation according to the modelling of VIMS night-side spectra by [Fletcher et al. \(2011a\)](#). They found that the best fits to the 4.6–5.1  $\mu\text{m}$  spectra were obtained with a compact cloud centred in the 2.5–2.8 bar region, and a second aerosol layer at  $p < 1.4$  bars, with the latter being 1.5–2 $\times$  more opaque in the summer hemisphere and mainly responsible for the observed asymmetry in 5- $\mu\text{m}$  emission. Whether the increased optical depths occurred in the putative diphosphine or ammonia layers could not be distinguished by the night-side observations, which lacked the constraints offered by reflected sunlight.

In contrast to the apparent independent behaviours of upper tropospheric optical depths and the deep cloud pressures inferred by [Fletcher et al. \(2011a\)](#) from mid-latitude night-side spectra, [Sromovsky et al. \(2020b\)](#) found in the south polar region that discrete bright features, produced mainly by increased optical depths in the ammonia layer, were also associated with the putative  $\text{NH}_4\text{SH}$  cloud tops being elevated to the 1.5–2 bar level. Averaging those elevated cloud pressures with the of 3–4 bars they inferred for the background clouds would put them closer to the zonal mean values of [Fletcher et al. \(2011a\)](#). However, there are other factors that might be affecting this pressure difference, including latitudinal differences in cloud structure, changes in VIMS calibration over time, and the use of different  $\text{He}/\text{H}_2$  ratios in temperature extrapolations.

#### 11.4.5 Aerosol Particle Shapes

Many aerosol models have successfully matched observations using spherical particle scattering properties as a way to parameterise the wavelength dependence of optical depth and phase functions, even though none of the particle layers

are expected to contain spherical particles. Mie scattering is the most common model assumption for the stratospheric haze layer, but polarisation measurements in the polar region indicate that fractal aggregates might be the real physical form of particles in these regions (West, 2014; Sayanagi et al., 2018). There is relatively uniform agreement that these stratospheric particles (when modelled as spheres) are in the range of 0.1-0.2  $\mu\text{m}$  in radius, with the larger particles found after longer exposure to sunlight. Pérez-Hoyos et al. (2016) used ISS observations over a wide range of phase angles to infer tropospheric layer phase functions, which they parameterised as double Henyey-Greenstein functions. They inferred that rather large (10- $\mu\text{m}$ ) particles may be present at low latitudes, with possibly 1- $\mu\text{m}$  particles at intermediate latitudes. Using models with spherical particle scattering yielded particle radius estimates ranging from tenths of a micron to 7  $\mu\text{m}$ , depending on the observational constraints used, time and space sampling, and assumed model structure (see Fig. 11.11). It remains to be understood what interpretation problems exist for models using spherical particle phase functions, which can fit the observations well over at least a small range of phase angles, but do not match the phase functions inferred by Pérez-Hoyos et al. (2016) for the upper troposphere from observations taken over a wide range of phase angles.

#### 11.4.6 Saturn's Chromophore

Seasonal aerosol variability is perhaps most directly observable in Saturn's visible colours, as revealed in Fig. 11.1. However, modellers disagree regarding the vertical location of aerosols responsible for Saturn's short-wavelength absorption, as indicated by the variety of yellow-orange layers in Fig. 11.11. The weight of evidence seems to favour short-wavelength absorption at least being present in the stratosphere, as that has been detected in short-wavelength observations by Cassini UVIS imaging near 180 nm (Pryor et al., 2019), as well as in UV HST observations (Karkoschka and Tomasko, 2005). There is also quite a variety in derived magnitudes of absorption, as illustrated in Fig. 11.13, which displays imaginary index versus wavelength derived for stratospheric and upper tropospheric layers (assuming spherical particles), and single-scattering albedo results for the upper troposphere (the only measure of absorption for double Henyey-Greenstein phase function models). Karkoschka and Tomasko (2005) found a large latitudinal variation in the magnitude of the imaginary index but not in its shape. Sromovsky et al. (2021) also found little spectral shape variation in the north polar hexagon region but a significant increase in amplitude between 2013 and 2016. There is a surprisingly large unexplained variability among the many results displayed in Fig. 11.13, which might be due to different model assumptions or spatial and/or temporal variations that have yet to be fully characterised.

#### 11.4.7 Vertical Extent of Aerosol Layers

There is also a lack of clear constraint on the vertical distribution of particles within each compositional layer. Early

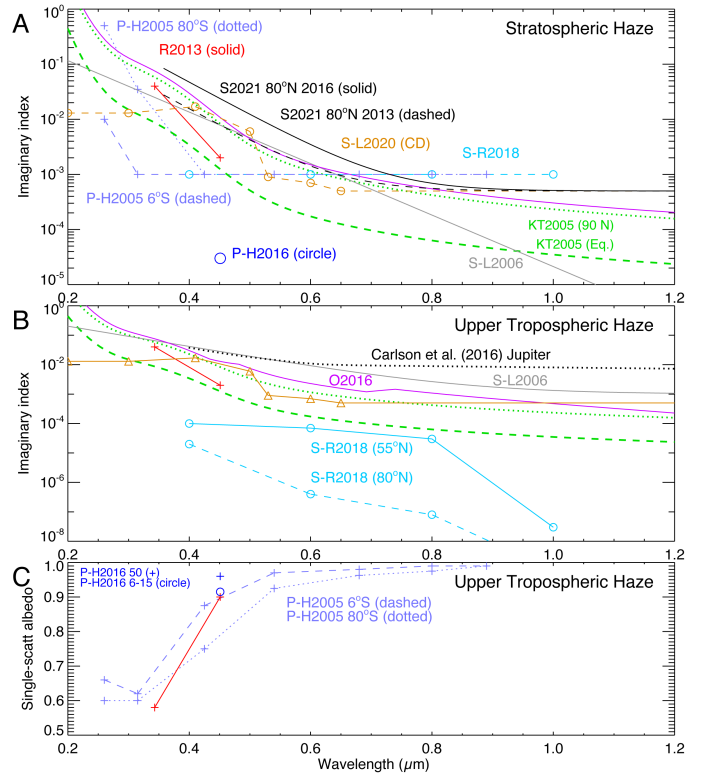


**Figure 11.13** Absorption properties of model chromophores for Saturn's stratosphere (A) and upper troposphere (B,C). Note the much slower falloff with wavelength of the Carlson et al. (2016) chromophore that has worked well for a variety of Jupiter observations. For explanations of the abbreviations, see Fig. 11.10.

models constrained by the CCD spectral range were successful with broad vertical distributions. But multiple compact layers, even in the stratosphere and upper troposphere, can also match observations, as illustrated by Sromovsky et al. (2020b,a, 2021). Evidence in favour of compact layers, at least in the south polar region, are evident from the presence of antishadows (Sromovsky et al., 2020a) because physically thin layers are required to produce them. Evidence for compact haze layers in the north polar region is their detection in 2015 ISS limb observations near the hexagon boundary (illustrated in Fig. 11.11) and analysed by Sánchez-Lavega et al. (2020), although it is not clear which of these layers have significant vertical optical depths (the fourth from the bottom shown in Fig. 11.11 appears to be the most prominent of the stratospheric layers). There have also been shadows observed in the north polar region (Ingersoll et al., 2018), but these seem to be more subtle for reasons that remain to be understood. Sromovsky et al. (2021) also showed that slightly better fits of north polar cloud structure can be obtained in some cases with thicker sheet clouds in which the top pressures are 60% of the bottom pressures (vs. the 90% they used generally). Thicker layers of the same optical depths would also reduce shadow contrast. More globally, compact layers also seem to be preferred by Fletcher et al. (2011a) for both deep and upper tropospheric layers, and at



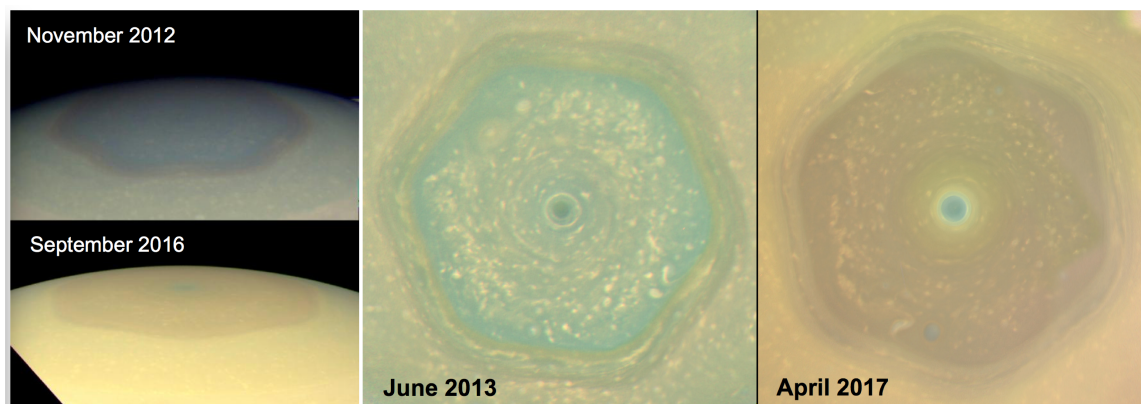


**Figure 11.14** Cassini ISS colour composite images documenting colour changes in Saturn's north polar region as it approached northern summer solstice. From [Sromovsky et al. \(2021\)](#).

least for the deep layer by [Barstow et al. \(2016\)](#), although these inferences lacked the additional constraints offered by observations in reflected sunlight.

#### 11.4.8 Seasonal Changes in the North Polar Region

Cassini ISS images between 2012 and 2017 (Fig. 11.14) document a significant change in the colour of the north polar region, from an initial blue/green colour throughout the interior of the hexagon, to a gold colour between the eye and the outer boundary of the hexagon (near  $75^\circ\text{N}$ ), but with little change seen within the eye ( $88.2^\circ$ – $90^\circ\text{N}$ ). VIMS observations in 2013 and 2016 (Fig. 11.15) helped to understand that evolution. Visual and Near-IR observations in combination (right panels of Fig. 11.15), show that the changes in visual colour are accompanied by much larger spectral changes at near-IR wavelengths. [Sromovsky et al. \(2021\)](#) employed both scattered sunlight and  $5\text{-}\mu\text{m}$  thermal emission to constrain their four-layer vertical structure model (see Fig. 11.11). They found that the colour change could be entirely explained by changes in the stratospheric haze, which included a  $2\times$  increase in particle radius, a  $5\times$  increase in optical depth, and a  $4\times$  increase in peak short-wavelength absorption, without any significant change in the shape of the absorption spectrum. They also found that the large increases at near-IR continuum wavelengths were mainly a result of large changes in the putative diphosphine layer (centred at 250–285 mbar), including a  $2\times$  increase in particle radius, and a  $5\times$  increase in optical depth. The ammonia layer changes were not quite as large, but important in explaining the changes seen in the  $3\text{-}\mu\text{m}$  region. Very little change was seen within the eye, either at visible or near-IR wavelengths, with low optical depths persisting. Apparently the increased sunlight that seemed to cause substantial change in the stratospheric haze throughout most of the hexagon interior, had little impact within the eye, which has a sharp boundary perhaps due to some dynamical transition that is also marked by a downwelling that would inhibit formation of aerosol layers. This is consistent with the thermal-IR inference of downwelling within the north polar cyclone by [Fletcher et al. \(2008\)](#). The blue/green to gold transition is also seen with lower contrast over a wide latitudinal range, in which the winter mid latitudes attain a slightly blueish

cast, which fades to a more gold/yellow colour on exposure to sunlight (illustrated by Fig. 11.1).

[Sromovsky et al. \(2021\)](#) also indicate the first potential temporal changes in phosphine, previously alluded to in Section 11.3. Parameterising the vertical profile of  $\text{PH}_3$  as a uniform mixing ratio up to a transition pressure, above which the mixing ratio decreased with altitude, they found that in a region between outer edge of the eye and the outer edge of the hexagon, the transition pressure was near to the pressure of the putative diphosphine cloud in 2016, but was much deeper in 2013, when that cloud had a much lower optical depth. Within the eye itself, the transition point was found to be deeper than the surroundings in both 2013 and 2016, while the deep abundance of phosphine was found to be  $\sim 30\%$  higher inside the eye than outside. At higher altitudes in the upper troposphere, the combined effect of these parameters was to make the upper-tropospheric  $\text{PH}_3$  abundance appear to be lower inside the eye, consistent with thermal-infrared studies ([Fletcher et al., 2008](#)).

#### 11.4.9 Summary of Aerosol Variability

Much has been learned about the latitudinal distribution and seasonal forcing of Saturn's aerosol layers, as well as their behaviour in localised storm regions, and some progress has been made in identifying aerosol composition. It is now reasonably clear that there are four compositionally distinct aerosol layers accessible to observations at UV to thermal infrared wavelengths. Underneath a stratospheric UV-absorbing haze is a putative diphosphine layer that is effective at obscuring an underlying ammonia ice layer, except in polar regions, where the putative  $\text{P}_2\text{H}_4$  layer is relatively translucent, and where Cassini/VIMS observations have made a strong case for the presence of ammonia ice, previously identified only in storm systems. The deeper putative  $\text{NH}_4\text{SH}$  layer expected from ECCM models seems to be present but in combination with some other absorber.

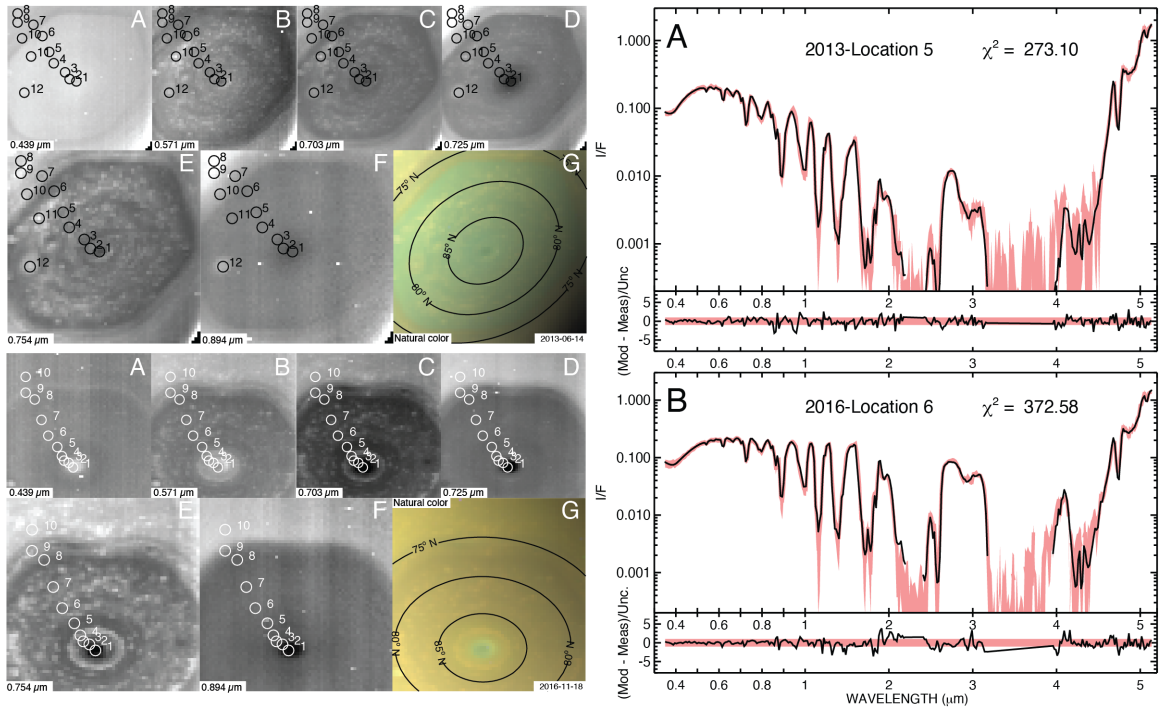


**Figure 11.15** Left: sample VIMS visual image planes and computed true colour image for June 2013 (top) and for November 2016 (bottom). Right: sample mid-hexagon spectra (coloured band width indicating uncertainty) from corresponding years and best-fit model spectra (solid black), with fit-difference/uncertainty plotted under each spectrum. From [Sromovsky et al. \(2021\)](#).

The tropospheric aerosols located at pressures less than 1.4 bar appear to undergo a seasonal variation, inferred from a hemispheric asymmetry in their obscuration of Saturn’s 5- $\mu\text{m}$  emission, though we still do not know whether that variation is in the putative diphosphine or ammonia ice layers. This variation may be partially responsible for the temperature perturbation discussed in Section 11.2 and Fig. 11.6, which is a radiative effect associated with these seasonally-variable aerosol layers.

The seasonal colour changes in the north polar region are now better understood. Except for the eye of the north polar cyclone, the stratospheric, putative diphosphine, and ammonia ice layers all became significantly optically thicker as they were exposed to increasing sunlight between 2012 and 2017. This caused a colour change from blue/green to gold, which is at least superficially similar to the observed hemispheric colour changes and those changes inferred from Hubble observations ([Karkoschka and Tomasko, 2005](#)). Nevertheless, we still have much to learn about the global-scale aerosol variability away from the polar domain. Many Cassini datasets have only just begun to be exploited, including the full spectral range of VIMS observations over wider spans of latitude and time, in addition to the ISS imaging and polarisation measurements. The connection between physical reality and parameterised models is currently somewhat uncertain, and while more extensive analysis of existing observations will help greatly, they will also need the support of laboratory investigations (a key priority is measuring the optical properties of diphosphine), photochemical and microphysical modeling, and ultimately suitable *in situ* observations.

## 11.5 Conclusions and Outstanding Questions

Throughout Cassini’s 13-year mission, its remote sensing experiments observed seasonal asymmetries in temperatures, atmospheric composition, and aerosols, and had begun to track how these asymmetries evolved as a function of time. As was made clear in the discussion of radiative climate models (Section 11.2), photochemical models (Section 11.3.3), and general circulation models, the seasonal trends are driven by insolation (to first order), but can be radically altered by the influence of dynamics, which in turn responds to contrasts in temperature. The circulation of the upper troposphere and stratosphere is likely to vary on seasonal timescales — from the seasonally-reversing Hadley cell at the equator with its interhemispheric transport ([Guerlet et al., 2009](#); [Friedson and Moses, 2012](#); [Bardet et al., 2022](#)), to the formation and dissipation of stratospheric polar vortices ([Fletcher et al., 2008, 2018a](#)), to the slow descent of temperature, wind (and potentially compositional) anomalies associated with Saturn’s Equatorial Stratospheric Oscillation ([Fouchet et al., 2008](#); [Orton et al., 2008](#); [Fletcher et al., 2017](#); [Guerlet et al., 2018](#); [Bardet et al., 2021](#)).

To understand how reproducible these dynamic perturbations are from Saturn-year to Saturn-year requires multiple decades of observations, exceeding the orbital period of Saturn (29.5 years). Intriguingly, observations of the equatorial region one Saturnian year apart, from Voyager to Cassini ([Sinclair et al., 2014](#); [Li et al., 2013](#); [Fletcher et al., 2016](#);

Blake et al., 2022), have suggested that the equatorial oscillation was not in the same phase (and therefore may not be semi-annual after all). In 2011–2013 the oscillation was substantially disrupted by the mid-latitude ‘stratospheric beacon’ that was produced by the Great White Storm (Fletcher et al., 2012, 2017; Guerlet et al., 2018; Sanchez-Lavega et al., 2018), and the tropospheric aftermath of that storm (in terms of temperatures and aerosols) was apparent right until the end of the Cassini time series (Achterberg et al., 2014; Fletcher et al., 2016), raising the question of whether sporadic storm eruptions could be a driver of interannual variability.

Efforts are now underway to understand interannual variability by comparing the Cassini record of temperatures, hydrocarbons, and aerosols (2004–2017) to ground-based observations since the 1980s and into the 2020s (Blake et al., 2022). Fig. 11.16 shows a montage of mid-infrared imaging of Saturn from 2004 to 2020, acquired by Keck (Orton and Yanamandra-Fisher, 2005), Subaru (Fletcher et al., 2009c) and the Very Large Telescope (Fletcher et al., 2017) in narrow-band filters sensing stratospheric methane emission ( $7.9\ \mu\text{m}$ ) and the tropospheric  $\text{H}_2\text{-He}$  continuum ( $17.6\ \mu\text{m}$ ). These provide the means to crudely determine the vertical temperature structure across the Earth-facing hemisphere, tracking the evolution of the banded structure and seasonal asymmetries as a function of time (Blake et al., 2022). These are supported by spatially-resolved spectral maps from the TEXES instrument mounted on Gemini (Guerlet et al., 2017), and Fig. 11.17 demonstrates the accuracy with which Saturn’s meridional stratospheric temperature gradient can be derived from these spectra, in comparison with CIRS observations taken nearby in time. Both the imaging and spectroscopic datasets reveal that we can now do from the ground what was only previously possible from space, at least for the Earth-facing hemisphere. Visible and infrared observations of this type will support forthcoming observations from the James Webb Space Telescope (Norwood et al., 2016), which launched in 2021.

Observations since 2017 extend the legacy of Cassini’s exploration into a completely new season — northern summer — for the first time. Unfortunately, the Earth-based vantage point will only ever be able to access the sunlit hemisphere, so the winter hemisphere will be obscured in darkness for a generation, until some future orbital mission once again reaches Saturn. Until then, scientists will monitor the evolution of temperature, composition, and aerosols through northern autumnal equinox (2025,  $L_s = 180^\circ$ ) and on to southern summer solstice (2032,  $L_s = 270^\circ$ ), completing the seasonal study through to the “one-Saturn-year anniversary” of Cassini’s arrival ( $L_s = 293^\circ$ ) in 2034. Such studies may allow us to address the following open questions:

- How do aerosols, transport of photochemical products, and meridional circulation contribute to Saturn’s seasonal temperature gradients?
- What processes drive belt/zone contrasts in temperature, aerosols, and composition, and what causes the decay of the zonal winds with altitude?
- What processes govern the dynamical evolution of Saturn’s equatorial oscillation? It is mainly seasonally forced

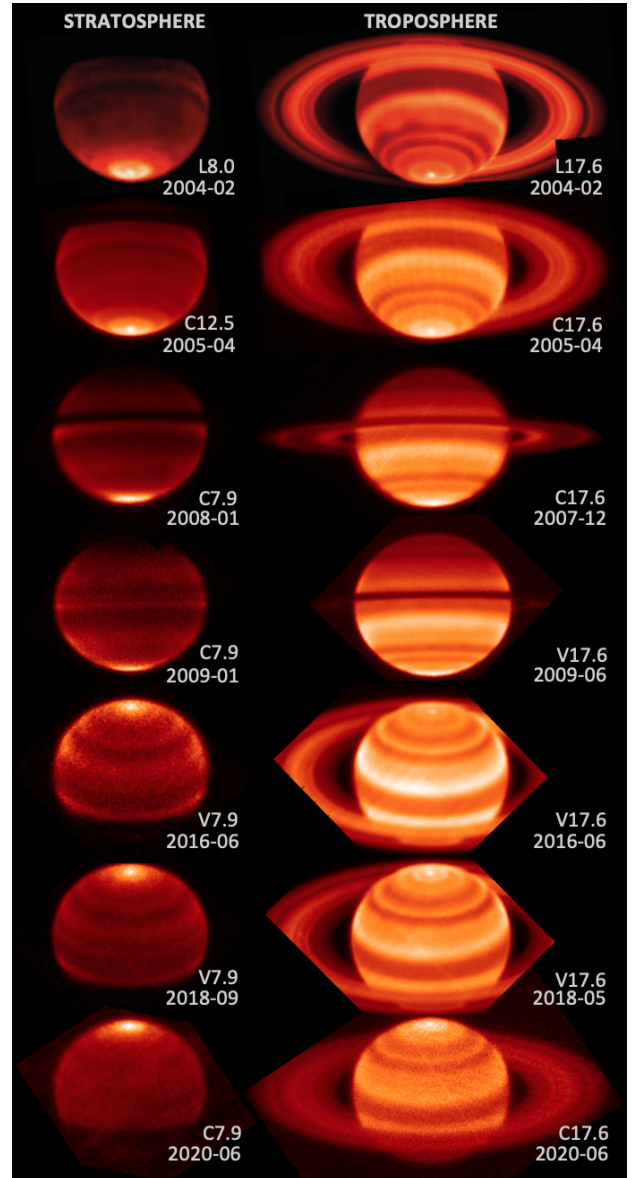


**Figure 11.16** Thermal images of Saturn from 2004 to 2020 adapted from Blake et al. (2022), as observed by three 8m+ ground-based observatories: L for Keck/LWS observations in 2004 (Orton and Yanamandra-Fisher, 2005), C for Subaru/COMICS (Fletcher et al., 2009c), and V for VLT/VISIR. Stratospheric images were typically acquired at  $7.9\text{--}8.0\ \mu\text{m}$  sensing stratospheric methane, with the exception of the 2005 observations at  $12.5\ \mu\text{m}$  sensing stratospheric ethane. Tropospheric images were acquired at  $17.6\ \mu\text{m}$ .

(like the semi-annual oscillation on Earth) or is it also shaped by variations in meteorological activity?

- What is the deep distribution of gases below Saturn’s visible cloud layers, and how do the belts and zones (and their associated wind/temperature gradients) vary with depth?
- What controls the formation, colouration, and vertical distribution of aerosols, and what are these aerosols made of?



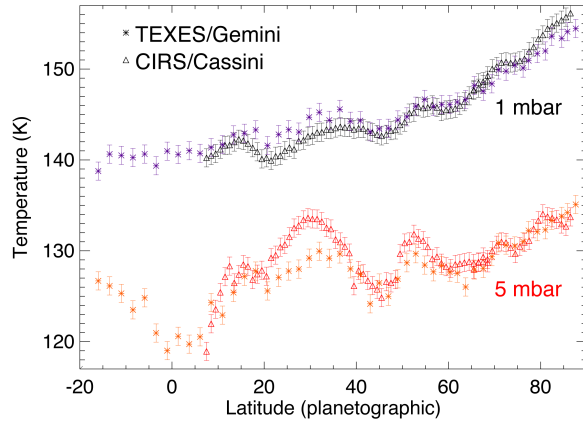


**Figure 11.17** Comparison of stratospheric temperature contrasts in Saturn's northern spring between Cassini/CIRS nadir observations in January-February 2017 (triangles) and Gemini/TEXES ground-based observations in March 2017 (crosses) at 1 mbar (top) and 5 mbar (bottom) (Guerlet et al., 2017).

- How do Saturn's auroras influence polar chemistry, aerosol formation, and heating?
- How is the circulation of the ionosphere and thermosphere connected to seasonal contrasts in Saturn's stratosphere?
- What determines the difference in meridional trends between  $C_2H_2$  and  $C_2H_6$ , and how do photochemical species vary with latitude/time at high stratospheric altitudes?

Seasonal exploration requires the continued development of new modelling tools. Since our last review (Fletcher et al., 2018b), we have seen the combination of stratospheric photochemistry and radiative climate models (Hue et al., 2016) and the combination of radiative calculations with general circulation models (Friedson and Moses, 2012; Guerlet et al., 2014; Spiga et al., 2020), but no attempts to date to combine all three into a self-consistent scheme. Tropospheric photochemical modelling (particularly in relation to  $PH_3$  and, to a lesser extent,  $NH_3$ ) remains in its infancy, with the relationship to the seasonal variability of upper-tropospheric and stratospheric hazes remaining to be explored. Microphysical modelling of cloud formation and precipitation, beyond the simplistic assumptions of thermochemical equilibrium cloud condensation, needs to be incorporated into circulation and chemistry models as active ingredients to understand the complex feedback between dynamics, chemistry, and cloud formation. Furthermore, the remote sensing measurements require a greater degree of consistency than is typically provided by individual studies in restricted wavelength ranges. Progress has been made in combining visible and near-infrared spectroscopy (from ISS and VIMS, Sromovsky et al., 2021), but this needs to be extended to thermal wavelengths (CIRS) and ultraviolet wavelengths (UVIS). Microwave measurements of Saturn provide insights into the connection between the upper troposphere and the deeper layers below the clouds (Janssen et al., 2013), but they remain underutilised, and could be continued from ground-based facilities like ALMA and the VLA. Our char-

acterisation of this seasonal giant, using both existing data and future measurements, will entail a broad combination of techniques and there are no shortages of opportunities for future research.

## Acknowledgements

Fletcher was supported by a Royal Society Research Fellowship and European Research Council Consolidator Grant (under the European Union's Horizon 2020 research and innovation programme, grant agreement No 723890) at the University of Leicester. Moses was supported by NASA Solar System Workings grant 80NSSC20K0462. Sromovsky was supported by NASA Cassini Data Analysis Program grants 80NSSC18K0966 and 80NSSC22K0339. The authors thank A.J. Friedson and M. Sylvestre for providing their data for the figures in this review.

## References

- Achterberg, R. K., Gierasch, P. J., Conrath, B. J., et al. 2014. Changes to Saturn's Zonal-mean Tropospheric Thermal Structure after the 2010-2011 Northern Hemisphere Storm. *ApJ*, **786**(May), 92.
- Atreya, S. K., and Wong, A.-S. 2005. Coupled Clouds and Chemistry of the Giant Planets – A Case for Multiprobes. *Space Sci. Rev.*, **116**(Jan.), 121–136.
- Badman, S. V., Achilleos, N., Baines, K. H., et al. 2011. Location of Saturn's northern infrared aurora determined from Cassini VIMS images. *Geophys. Res. Lett.*, **38**(Feb.), L03102.
- Baines, K. H., Momary, T. W., Roos-Serote, M., et al. 2006. North vs South on Saturn: Discovery of a Pronounced Hemispherical Asymmetry in Saturn's 5-Micron Emission and Associated Deep Cloud Structure by Cassini/VIMS. *B.A.A.S.*, **38**, 488.
- Baines, K. H., Sromovsky, L. A., Fry, P. M., et al. 2018. The Eye of Saturn's North Polar Vortex: Unexpected Cloud Structures Observed at High Spatial Resolution by Cassini/VIMS. *Geophys. Res. Lett.*, **45**(12), 5867–5875.
- Bardet, Deborah, Spiga, Aymeric, Guerlet, Sandrine, et al. 2021. Global climate modeling of Saturn's atmosphere. Part IV: Stratospheric equatorial oscillation. *Icarus*, **354**(Jan.), 114042.
- Bardet, Deborah, Spiga, Aymeric, and Guerlet, Sandrine. 2022. Joint evolution of equatorial oscillation and interhemispheric circulation in Saturn's stratosphere. *Nature Astronomy*, **6**(May), 804–811.
- Barstow, J. K., Irwin, P. G. J., Fletcher, L. N., et al. 2016. Probing Saturn's tropospheric cloud with Cassini/VIMS. *Icarus*, **271**(June), 400–417.
- Blake, J. S. D., Fletcher, L. N., Orton, G. S., et al. 2022. Saturn's Seasonal Variability from Four Decades of Ground-Based Mid-Infrared Observations. *Icarus*, Nov.
- Brown, Z., Koskinen, T., Müller-Wodarg, I., et al. 2020. A pole-to-pole pressure-temperature map of Saturn's thermosphere from Cassini Grand Finale data. *Nature Astronomy*, **4**(Apr.), 872–879.
- Brown, Zarah L., Medvedev, Alexander S., Starichenko, Ekaterina D., et al. 2022. Evidence for Gravity Waves in the



- Thermosphere of Saturn and Implications for Global Circulation. *Geophysical Research Letters*, **49**(8), e97219.
- Carlson, R. W., Baines, K. H., Anderson, M. S., et al. 2016. Chromophores from photolyzed ammonia reacting with acetylene: Application to Jupiter's Great Red Spot. *Icarus*, **274**(Aug.), 106–115.
- Cassidy, T. A., and Johnson, R. E. 2010. Collisional spreading of Enceladus' neutral cloud. *Icarus*, **209**(2), 696–703.
- Cavalié, T., Hartogh, P., Billebaud, F., et al. 2010. A cometary origin for CO in the stratosphere of Saturn? *Astron. Astrophys.*, **510**(Feb.), A88+.
- Cavalié, T., Dobrijevic, M., Fletcher, L. N., et al. 2015. Photochemical response to the variation of temperature in the 2011–2012 stratospheric vortex of Saturn. *Astron. Astrophys.*, **580**(Aug.), A55.
- Cavalié, T., Hue, V., Hartogh, P., et al. 2019. Herschel map of Saturn's stratospheric water, delivered by the plumes of Enceladus. *Astron. Astrophys.*, **630**(Oct.), A87.
- Cavalié, T., Benmahi, B., Hue, V., et al. 2021. First direct measurement of auroral and equatorial jets in the stratosphere of Jupiter. *Astron. Astrophys.*, **647**(Mar.), L8.
- Cess, R. D., and Caldwell, J. 1979. A Saturnian stratospheric seasonal climate model. *Icarus*, **38**, 349–357.
- Conrath, B. J., and Pirraglia, J. A. 1983. Thermal structure of Saturn from Voyager infrared measurements - Implications for atmospheric dynamics. *Icarus*, **53**, 286–292.
- Conrath, B. J., Gierasch, P. J., and Leroy, S. S. 1990. Temperature and circulation in the stratosphere of the outer planets. *Icarus*, **83**, 255–281.
- Conrath, B. J., Gierasch, P. J., and Ustinov, E. A. 1998. Thermal Structure and Para Hydrogen Fraction on the Outer Planets from Voyager IRIS Measurements. *Icarus*, **135**, 501–517.
- Del Genio, A. D., Achterberg, R. K., Baines, K. H., et al. 2009. *Saturn Atmospheric Structure and Dynamics*, In: *Saturn from Cassini-Huygens*. Springer. Chap. 6, pages 113–159.
- Dobrijevic, M., Ollivier, J. L., Billebaud, F., et al. 2003. Effect of chemical kinetic uncertainties on photochemical modeling results: Application to Saturn's atmosphere. *Astron. Astrophys.*, **398**(Jan.), 335–344.
- Dobrijevic, M., Cavalié, T., and Billebaud, F. 2011. A methodology to construct a reduced chemical scheme for 2D–3D photochemical models: Application to Saturn. *Icarus*, **214**, 275–285.
- Dougherty, M. K., Khurana, K. K., Neubauer, F. M., et al. 2006. Identification of a Dynamic Atmosphere at Enceladus with the Cassini Magnetometer. *Science*, **311**(5766), 1406–1409.
- Dougherty, Michele K., Cao, Hao, Khurana, Krishan K., et al. 2018. Saturn's magnetic field revealed by the Cassini Grand Finale. *Science*, **362**(6410), aat5434.
- Dowling, T. E., Greathouse, T. K., Sussman, M. G., et al. 2010 (Oct.). New Radiative Transfer Capability in the EPIC Atmospheric Model with Application to Saturn and Uranus. Page 1021 of: *AAS/Division for Planetary Sciences Meeting Abstracts #42*. Bulletin of the American Astronomical Society, vol. 42.
- Dyudina, U.A., Ingersoll, A.P., Ewald, S.P., et al. 2007. Lightning storms on Saturn observed by Cassini ISS and RPWS during 2004–2006. *Icarus*, **190**(2), 545–555.
- Dyudina, Ulyana A., Ingersoll, Andrew P., Ewald, Shawn P., et al. 2013. Saturn's visible lightning, its radio emissions, and the structure of the 2009–2011 lightning storms. *Icarus*, **226**(Sep), 1020–1037.
- Feuchtgruber, H., Lellouch, E., de Graauw, T., et al. 1997. External supply of oxygen to the atmospheres of giant planets. *Nature*, **389**(Sept.), 159–162.
- Flasar, F. M., Kunde, V. G., Abbas, M. M., et al. 2004. Exploring The Saturn System In The Thermal Infrared: The Composite Infrared Spectrometer. *Space Science Reviews*, **115**, 169–297.
- Fleshman, B. L., Delamere, P. A., Bagenal, F., et al. 2012. The roles of charge exchange and dissociation in spreading Saturn's neutral clouds. *Journal of Geophysical Research (Planets)*, **117**(E5), E05007.
- Fletcher, L. N., Irwin, P. G. J., Teanby, N. A., et al. 2007. Characterising Saturn's Vertical Temperature Structure from Cassini/CIRS. *Icarus*, **189**, 457–478.
- Fletcher, L. N., Irwin, P. G. J., Orton, G. S., et al. 2008. Temperature and Composition of Saturn's Polar Hot Spots and Hexagon. *Science*, **319**(Jan.), 79–82.
- Fletcher, L. N., Orton, G. S., Teanby, N. A., et al. 2009a. Methane and its isotopologues on Saturn from Cassini/CIRS observations. *Icarus*, **199**(Feb.), 351–367.
- Fletcher, L. N., Orton, G. S., Teanby, N. A., et al. 2009b. Phosphine on Jupiter and Saturn from Cassini/CIRS. *Icarus*, **202**(Aug.), 543–564.
- Fletcher, L. N., Orton, G. S., Yanamandra-Fisher, P., et al. 2009c. Retrievals of atmospheric variables on the gas giants from ground-based mid-infrared imaging. *Icarus*, **200**(Mar.), 154–175.
- Fletcher, L. N., Achterberg, R. K., Greathouse, T. K., et al. 2010. Seasonal change on Saturn from Cassini/CIRS observations, 2004–2009. *Icarus*, **208**(July), 337–352.
- Fletcher, L. N., Baines, K. H., Momary, T. W., et al. 2011a. Saturn's tropospheric composition and clouds from Cassini/VIMS 4.6–5.1  $\mu\text{m}$  nightside spectroscopy. *Icarus*, **214**(Aug.), 510–533.
- Fletcher, L. N., Hesman, B. E., Irwin, P. G. J., et al. 2011b. Thermal Structure and Dynamics of Saturn's Northern Springtime Disturbance. *Science*, **332**(June), 1413–1417.
- Fletcher, L. N., Hesman, B. E., Achterberg, R. K., et al. 2012. The origin and evolution of Saturn's 2011–2012 stratospheric vortex. *Icarus*, **221**(Nov.), 560–586.
- Fletcher, L. N., Irwin, P. G. J., Sinclair, J. A., et al. 2015. Seasonal Evolution of Saturn's Polar Temperatures and Composition. *Icarus*, **250**, 131–153.
- Fletcher, L. N., Irwin, P. G. J., Achterberg, R. K., et al. 2016. Seasonal variability of Saturn's tropospheric temperatures, winds and para-H<sub>2</sub> from Cassini far-IR spectroscopy. *Icarus*, **264**(Jan.), 137–159.
- Fletcher, L. N., Guerlet, S., Orton, G. S., et al. 2017. Disruption of Saturn's quasi-periodic equatorial oscillation by the Great Northern Storm. *Nature Astronomy*, **1**(Nov.), 765–770.
- Fletcher, L. N., Orton, G. S., Sinclair, J. A., et al. 2018a. A hexagon in Saturn's northern stratosphere surrounding the emerging summertime polar vortex. *Nature Communications*, **9**(Sept.), 3564.
- Fletcher, L. N., Greathouse, T. K., Moses, J. I., et al. 2018b. *Saturn's Seasonally Changing Atmosphere: Thermal Structure, Composition and Aerosols*. Cambridge Planetary Science. Cambridge Univ. Press, New York. Chap. 10.
- Fletcher, Leigh N., Kaspi, Yohai, Guillot, Tristan, et al. 2020. How Well Do We Understand the Belt/Zone Circulation of Giant Planet Atmospheres? *Space Science Reviews*, **216**(2), 30.

- Fouchet, T., Lellouch, E., and Feuchtgruber, H. 2003. The hydrogen ortho-to-para ratio in the stratospheres of the giant planets. *Icarus*, **161**, 127–143.
- Fouchet, T., Guerlet, S., Strobel, D.F., et al. 2008. An equatorial oscillation in Saturn’s middle atmosphere. *Nature*, **453**(7192), 200–202.
- Fouchet, T., Moses, J. I., and Conrath, B. J. 2009. *Saturn: Composition and Chemistry*, In: *Saturn from Cassini-Huygens*. Chap. 5, pages 83–.
- Friedson, A. J., and Moses, J. I. 2012. General circulation and transport in Saturn’s upper troposphere and stratosphere. *Icarus*, **218**(Apr.), 861–875.
- Gezari, D. Y., Mumma, M. J., Espenak, F., et al. 1989. New features in Saturn’s atmosphere revealed by high-resolution thermal infrared images. *Nature*, **342**, 777–780.
- Gillet, F. C., and Orton, G. S. 1975. Center-to-limb observations of Saturn in the thermal infrared. *Astrophys. J.*, **195**(Jan.), L47–L49.
- Greathouse, T., Moses, J., Fletcher, L., et al. 2010 (May). Seasonal Temperature Variations in Saturn’s Stratosphere: Radiative Seasonal Model vs. Observations. Page 4806 of: *EGU General Assembly Conference Abstracts*. EGU General Assembly Conference Abstracts, vol. 12.
- Greathouse, T. K., Lacy, J. H., Bézard, B., et al. 2005. Meridional variations of temperature,  $C_2H_2$  and  $C_2H_6$  abundances in Saturn’s stratosphere at southern summer solstice. *Icarus*, **177**, 18–31.
- Guerlet, S., Fouchet, T., Bézard, B., et al. 2009. Vertical and meridional distribution of ethane, acetylene and propane in Saturn’s stratosphere from CIRS/Cassini limb observations. *Icarus*, **203**, 214–232.
- Guerlet, S., Fouchet, T., Bézard, B., et al. 2010. Meridional distribution of  $CH_3C_2H$  and  $C_4H_2$  in Saturn’s stratosphere from CIRS/Cassini limb and nadir observations. *Icarus*, **209**(Oct.), 682–695.
- Guerlet, S., Spiga, A., Sylvestre, M., et al. 2014. Global climate modeling of Saturn’s atmosphere. Part I: Evaluation of the radiative transfer model. *Icarus*, **238**(Aug.), 110–124.
- Guerlet, S., Fouchet, T., Vinatier, S., et al. 2015. Stratospheric benzene and hydrocarbon aerosols detected in Saturn’s auroral regions. *A&A*, **580**(Aug.), A89.
- Guerlet, S., Fouchet, T., Spiga, A., et al. 2018. Equatorial Oscillation and Planetary Wave Activity in Saturn’s Stratosphere Through the Cassini Epoch. *Journal of Geophysical Research (Planets)*, **123**(1), 246–261.
- Guerlet, Sandrine, Greathouse, Thomas K., Orton, Glenn S., et al. 2017 (Oct.). Saturn’s stratospheric temperature and composition at the epoch of the 2017 summer solstice. Page 209.04 of: *AAS/Division for Planetary Sciences Meeting Abstracts #49*. AAS/Division for Planetary Sciences Meeting Abstracts.
- Hanel, R., Conrath, B., Flasar, F. M., et al. 1981. Infrared observations of the Saturnian system from Voyager 1. *Science*, **212**, 192–200.
- Hanel, R., Conrath, B., Flasar, F. M., et al. 1982. Infrared observations of the Saturnian system from Voyager 2. *Science*, **215**, 544–548.
- Hartogh, P., Lellouch, E., Moreno, R., et al. 2011. Direct detection of the Enceladus water torus with Herschel. *Astron. Astrophys.*, **532**(Aug.), L2+.
- Hedman, M. M. 2019. Bright clumps in the D68 ringlet near the end of the Cassini Mission. *Icarus*, **323**(May), 62–75.
- Hesman, B. E., Jennings, D. E., Sada, P. V., et al. 2009. Saturn’s latitudinal  $C_2H_2$  and  $C_2H_6$  abundance profiles from Cassini/CIRS and ground-based observations. *Icarus*, **202**(July), 249–259.
- Hesman, B. E., Bjoraker, G. L., Sada, P. V., et al. 2012. Elusive Ethylene Detected in Saturn’s Northern Storm Region. *Astrophys. J.*, **760**(1), 24.
- Holton, J.R. 2004. *An Introduction to Dynamic Meteorology*. Academic press.
- Howett, C., Irwin, P., Calcutt, S., et al. 2005. Latitudinal variations of acetylene and ethane in the stratosphere of Saturn from Cassini/CIRS observations. Page 657 of: *Bulletin of the American Astronomical Society*.
- Hue, V., Cavalié, T., Dobrijevic, M., et al. 2015. 2D photochemical modeling of Saturn’s stratosphere. Part I: Seasonal variation of atmospheric composition without meridional transport. *Icarus*, **257**(Sept.), 163–184.
- Hue, V., Greathouse, T. K., Cavalié, T., et al. 2016. 2D photochemical modeling of Saturn’s stratosphere. Part II: Feedback between composition and temperature. *Icarus*, **267**(Mar.), 334–343.
- Hue, V., Hersant, F., Cavalié, T., et al. 2018. Photochemistry, mixing and transport in Jupiter’s stratosphere constrained by Cassini. *Icarus*, **307**(June), 106–123.
- Hurley, J., Fletcher, L. N., Irwin, P. G. J., et al. 2012. Latitudinal variation of upper tropospheric  $NH_3$  on Saturn derived from Cassini/CIRS far-infrared measurements. *Plan. & Space Sci.*, **73**(Dec.), 347–363.
- Ingersoll, Andrew P., Ewald, Shawn P., Sayanagi, Kunio M., et al. 2018. Saturn’s Atmosphere at 1–10 Kilometer Resolution. *Geophys. Res. Lett.*, **45**(15), 7851–7856.
- Janssen, M. A., Ingersoll, A. P., Allison, M. D., et al. 2013. Saturn’s thermal emission at 2.2-cm wavelength as imaged by the Cassini RADAR radiometer. *Icarus*, **226**(Sept.), 522–535.
- Johnson, R. E., Melin, H., Stallard, T. S., et al. 2018. Mapping  $H_3^+$  Temperatures in Jupiter’s Northern Auroral Ionosphere Using VLT-CRILES. *Journal of Geophysical Research (Space Physics)*, **123**(7), 5990–6008.
- Karkoschka, E., and Tomasko, M. 2005. Saturn’s vertical and latitudinal cloud structure 1991–2004 from HST imaging in 30 filters. *Icarus*, **179**, 195–221.
- Karkoschka, E., and Tomasko, M. G. 1992. Saturn’s upper troposphere 1986–1989. *Icarus*, **97**, 161–181.
- Kaye, J. A., and Strobel, D. F. 1984. Phosphine photochemistry in the atmosphere of Saturn. *Icarus*, **59**(Sept.), 314–335.
- Kerola, D. X., Larson, H. P., and Tomasko, M. G. 1997. Analysis of the Near-IR Spectrum of Saturn: A Comprehensive Radiative Transfer Model of Its Middle and Upper Troposphere. *Icarus*, **127**, 190–212.
- Koskinen, T. T., Sandel, B. R., Yelle, R. V., et al. 2015. Saturn’s variable thermosphere from Cassini/UVIS occultations. *Icarus*, **260**(Nov.), 174–189.
- Koskinen, T. T., Moses, J. I., West, R. A., et al. 2016. The detection of benzene in Saturn’s upper atmosphere. *Geophys. Res. Lett.*, **43**(Aug.), 7895–7901.
- Laraia, A. L., Ingersoll, A. P., Janssen, M. A., et al. 2013. Analysis of Saturn’s thermal emission at 2.2-cm wavelength: Spatial distribution of ammonia vapor. *Icarus*, **226**(Sept.), 641–654.
- Li, L., Conrath, B. J., Gierasch, P. J., et al. 2010. Saturn’s emitted power. *Journal of Geophysical Research (Planets)*, **115**(E14), 11002.
- Li, L., Achterberg, R. K., Conrath, B. J., et al. 2013. Strong Temporal Variation Over One Saturnian Year: From Voyager to Cassini. *Scientific Reports*, **3**(Aug.).

- Lindal, G. F., Sweetnam, D. N., and Eshleman, V. R. 1985. The atmosphere of Saturn - an analysis of the Voyager radio occultation measurements. *Astron. J.*, **90**, 1136–1146.
- Massie, S. T., and Hunten, D. M. 1982. Conversion of para and ortho hydrogen in the Jovian planets. *Icarus*, **49**, 213–226.
- Miller, K. E., Waite, J. H., Perryman, R. S., et al. 2020. Cassini INMS constraints on the composition and latitudinal fractionation of Saturn ring rain material. *Icarus*, **339**(Mar.), 113595.
- Moses, J. I., and Greathouse, T. K. 2005. Latitudinal and seasonal models of stratospheric photochemistry on Saturn: Comparison with infrared data from IRTF/TEXES. *Journal of Geophysical Research (Planets)*, **110**(Sept.), E09007.
- Moses, Julianne, Koskinen, Tommi, Guerlet, Sandrine, et al. 2018 (Oct.). The formation of benzene and complex hydrocarbons in the auroral and non-auroral regions of Saturn. Page 214.04 of: *AAS/Division for Planetary Sciences Meeting Abstracts #50*. AAS/Division for Planetary Sciences Meeting Abstracts, vol. 50.
- Moses, Julianne I., and Poppe, Andrew R. 2017. Dust ablation on the giant planets: Consequences for stratospheric photochemistry. *Icarus*, **297**(Nov.), 33–58.
- Moses, Julianne I., Armstrong, Eleanor S., Fletcher, Leigh N., et al. 2015. Evolution of stratospheric chemistry in the Saturn storm beacon region. *Icarus*, **261**(Nov.), 149–168.
- Moses, Julianne I., Brown, Zarah L., Koskinen, Tommi T., et al. 2023. Saturn's atmospheric response to the large influx of ring material inferred from Cassini INMS measurements. *Icarus*, **391**, 115328.
- Müller-Wodarg, I. C. F., Mendillo, M., Yelle, R. V., et al. 2006. A global circulation model of Saturn's thermosphere. *Icarus*, **180**(Jan.), 147–160.
- Müller-Wodarg, I. C. F., Koskinen, T. T., Moore, L., et al. 2019. Atmospheric Waves and Their Possible Effect on the Thermal Structure of Saturn's Thermosphere. *Geophys. Res. Lett.*, **46**(5), 2372–2380.
- Norwood, J., Moses, J., Fletcher, L. N., et al. 2016. Giant Planet Observations with the James Webb Space Telescope. *PASP*, **128**(1), 018005.
- O'Donoghue, J., Moore, L., Bhakypaibul, T., et al. 2021. Global upper-atmospheric heating on Jupiter by the polar aurorae. *Nature*, **596**(7870), 54–57.
- Oliva, F., Adriani, A., Moriconi, M. L., et al. 2016. Clouds and hazes vertical structure of a Saturn's giant vortex from Cassini/VIMS-V data analysis. *Icarus*, **278**(Nov.), 215–237.
- Orton, G. S., and Ingersoll, A. P. 1980. Saturn's atmospheric temperature structure and heat budget. *Journal of Geophysical Research*, **85**(Nov.), 5871–5881.
- Orton, G. S., and Yanamandra-Fisher, P. A. 2005. Saturn's Temperature Field from High-Resolution Middle-Infrared Imaging. *Science*, **307**, 696–698.
- Orton, G.S., Yanamandra-Fisher, P.A., Fisher, B.M., et al. 2008. Semi-annual oscillations in Saturn's low-latitude stratospheric temperatures. *Nature*, **453**(May), 196–198.
- Pérez-Hoyos, S., Sánchez-Lavega, A., French, R. G., et al. 2005. Saturn's cloud structure and temporal evolution from ten years of Hubble Space Telescope images (1994–2003). *Icarus*, **176**, 155–174.
- Pérez-Hoyos, Santiago, Sanz-Requena, José Francisco, Sánchez-Lavega, Agustín, et al. 2016. Saturn's tropospheric particles phase function and spatial distribution from Cassini ISS 2010–11 observations. *Icarus*, **277**(Oct.), 1–18.
- Poppe, A. R. 2016. An improved model for interplanetary dust fluxes in the outer Solar System. *Icarus*, **264**(Jan.), 369–386.
- Porco, C. C., Helfenstein, P., Thomas, P. C., et al. 2006. Cassini Observes the Active South Pole of Enceladus. *Science*, **311**(5766), 1393–1401.
- Pryor, W. R., Esposito, L. W., Jouchoux, A., et al. 2019. Cassini UVIS Detection of Saturn's North Polar Hexagon in the Grand Finale Orbits. *Journal of Geophysical Research (Planets)*, **124**(7), 1979–1988.
- Roman, M. T., Banfield, D., and Gierasch, P. J. 2013. Saturn's cloud structure inferred from Cassini ISS. *Icarus*, **225**(July), 93–110.
- Sánchez-Lavega, A., Hueso, R., Pérez-Hoyos, S., et al. 2006. A strong vortex in Saturn's South Pole. *Icarus*, **184**, 524–531.
- Sánchez-Lavega, A., del Río-Gaztelurrutia, T., Hueso, R., et al. 2011. Deep winds beneath Saturn's upper clouds from a seasonal long-lived planetary-scale storm. *Nature*, **475**(July), 71–74.
- Sanchez-Lavega, A., Fischer, G., Fletcher, L. N., et al. 2018. *The Great Saturn Storm of 2010–2011*. Cambridge Planetary Science. Cambridge Univ. Press, New York. Chap. 13.
- Sánchez-Lavega, A., García-Muñoz, A., del Río-Gaztelurrutia, T., et al. 2020. Multilayer hazes over Saturn's hexagon from Cassini ISS limb images. *Nature Communications*, **11**(May), 2281.
- Sanz-Requena, J. F., Pérez-Hoyos, S., Sánchez-Lavega, A., et al. 2018. Haze and cloud structure of Saturn's North Pole and Hexagon Wave from Cassini/ISS imaging. *Icarus*, **305**(May), 284–300.
- Sayanagi, K. M., Baines, K. H., Dyudina, U. A., et al. 2018. *Saturn's Polar Atmosphere*. Cambridge Planetary Science. Cambridge Univ. Press, New York. Chap. 12, pages 337–376.
- Serigano, J., Hörst, S. M., He, C., et al. 2022. Compositional Measurements of Saturn's Upper Atmosphere and Rings From Cassini INMS: An Extended Analysis of Measurements From Cassini's Grand Finale Orbits. *Journal of Geophysical Research (Planets)*, **127**(6), e07238.
- Sinclair, J. A., Irwin, P. G. J., Fletcher, L. N., et al. 2013. Seasonal variations of temperature, acetylene and ethane in Saturn's atmosphere from 2005 to 2010, as observed by Cassini-CIRS. *Icarus*, **225**(July), 257–271.
- Sinclair, J. A., Irwin, P. G. J., Fletcher, L. N., et al. 2014. From Voyager-IRIS to Cassini-CIRS: Interannual variability in Saturn's stratosphere? *Icarus*, **233**(May), 281–292.
- Sinclair, J. A., Orton, G. S., Fernandes, J., et al. 2019. A brightening of Jupiter's auroral 7.8- $\mu\text{m}$  CH<sub>4</sub> emission during a solar-wind compression. *Nature Astronomy*, **3**(Apr.), 607–613.
- Spiga, Aymeric, Guerlet, Sandrine, Millour, Ehouarn, et al. 2020. Global climate modeling of Saturn's atmosphere. Part II: Multi-annual high-resolution dynamical simulations. *Icarus*, **335**(Jan), 113377.
- Sromovsky, L. A., Baines, K. H., and Fry, P. M. 2013. Saturn's Great Storm of 2010–2011: Evidence for ammonia and water ices from analysis of VIMS spectra. *Icarus*, **226**(Sept.), 402–418.
- Sromovsky, L. A., Baines, K. H., Fry, P. M., et al. 2016. Cloud clearing in the wake of Saturn's Great Storm of 2010–2011 and suggested new constraints on Saturn's He/H<sub>2</sub> ratio. *Icarus*, **276**(Sept.), 141–162.
- Sromovsky, L. A., Baines, K. H., and Fry, P. M. 2018. Models of bright storm clouds and related dark ovals in Saturn's Storm Alley as constrained by 2008 Cassini/VIMS spectra. *Icarus*, **302**(Mar.), 360–385.
- Sromovsky, L. A., Fry, P. M., and Baines, K. H. 2020a. Interpretation of shadows and antishadows on Saturn and the

- evidence against south polar eyewalls. *Icarus*, **344**(July), 113399.
- Sromovsky, L. A., Baines, K. H., and Fry, P. M. 2020b. Saturn’s south polar cloud composition and structure inferred from 2006 Cassini/VIMS spectra and ISS images. *Icarus*, **344**(July), 113398.
- Sromovsky, L. A., Baines, K. H., and Fry, P. M. 2021. Evolution of Saturn’s north polar color and cloud structure between 2012 and 2017 inferred from Cassini VIMS and ISS observations. *Icarus*, **362**(July), 114409.
- Stam, D. M., Banfield, D., Gierasch, P. J., et al. 2001. Near-IR Spectrophotometry of Saturnian Aerosols-Meridional and Vertical Distribution. *Icarus*, **152**, 407–422.
- Sylvestre, M., Guerlet, S., Fouchet, T., et al. 2015. Seasonal changes in Saturn’s stratosphere inferred from Cassini/CIRS limb observations. *Icarus*, **258**(Sept.), 224–238.
- Vasavada, A. R., Hörst, S. M., Kennedy, M. R., et al. 2006. Cassini imaging of Saturn: Southern hemisphere winds and vortices. *Journal of Geophysical Research (Planets)*, **111**(E10), 5004.
- Visscher, C., Sperier, A. D., Moses, J. I., et al. 2009 (Mar.). Phosphine and ammonia photochemistry in Jupiter’s troposphere. Page 1201 of: *Lunar and Planetary Science Conference*. Lunar and Planetary Science Conference, vol. 40.
- Waite, J. H., Perryman, R. S., Perry, M. E., et al. 2018. Chemical interactions between Saturn’s atmosphere and its rings. *Science*, **362**(6410), aat2382.
- West, R. A. 2014. The UV hazes of Saturn. In: *Asia-Oceania GeoSciences Meeting, Sapporo, Japan*. Asia-Oceania GeoSciences Meeting, Sapporo, Japan.
- West, R. A., Orton, G. S., Draine, B. T., et al. 1989. Infrared absorption features for tetrahedral ammonia ice crystals. *Icarus*, **80**(July), 220–223.
- West, R. A., Baines, K. H., Karkoschka, E., et al. 2009. *Clouds and Aerosols in Saturn’s Atmosphere*, In: *Saturn from Cassini-Huygens*. Springer. Chap. 7, pages 161–179.
- Wong, A.-S., Lee, A. Y. T., Yung, Y. L., et al. 2000. Jupiter: Aerosol chemistry in the polar atmosphere. *Astrophys. J. Lett.*, **534**, L215–L217.
- Wong, A.-S., Yung, Y. L., and Friedson, A. J. 2003. Benzene and haze formation in the polar atmosphere of Jupiter. *Geophys. Res. Lett.*, **30**, 1447.
- Zhang, X., West, R. A., Banfield, D., et al. 2013. Stratospheric aerosols on Jupiter from Cassini observations. *Icarus*, **226**(Sept.), 159–171.